water

MDPI

Article

Degradation of Carbamazepine by HF-Free-Synthesized MIL-101(Cr)@Anatase TiO_2 Composite under UV-A Irradiation: Degradation Mechanism, Wastewater Matrix Effect, and Degradation Pathway

J. W. Goh [1], Y. Xiong [1], W. Wu [2], Z. Huang [2], S. L. Ong [1] and J. Y. Hu [1,*]

[1] Department of Civil & Environmental Engineering, National University of Singapore, 1 Engineering Drive 2, Singapore 117576, Singapore
[2] Singapore Institute of Manufacturing Technology, 2 Fusionopolis Way #08-04 Innovis, Singapore 138634, Singapore
* Correspondence: hujiangyong@nus.edu.sg

Abstract: TiO_2 has been hampered by drawbacks such as rapid photoelectron and hole recombination and a wide energy band gap of 3.2 eV. In this study, MIL-101(Cr)@TiO_2 was synthesised without any mineraliser (HF) as part of material modification approach to overcome those pitfalls. The composite was well characterized by XRD, FT-IR, TEM, XPS, BET, TGA, and Raman spectroscopy. Under optimal synthesis conditions, the 9.17% MIL-101(Cr)@TiO_2 composite exhibited 99.9% CBZ degradation after 60 min under UV-A irradiation. This can be attributed to the delayed recombination of photo-generated h^+ and e^- and a reduced band gap energy of 2.9 eV. A Type II heterojunction structure was proposed for the composite using the Mulligan function of electronegativity with the calculated E_{cb} and E_{vb}. Besides, trapping experiments and ESR spectroscopy confirmed $O_2^{\bullet-}$ as the main ROS for CBZ degradation. The effects of the operating parameters such as pH, UV intensity, composite dosage, and initial pollutant concentration were also evaluated. The scavenging effects of inorganic and organic constituents of pharmaceutical wastewater on the process were also evaluated, with HCO_3^-, CO_3^{2-}, and THF having more significant inhibition on the overall CBZ degradation. The degradation pathways of CBZ were also proposed based on detected intermediates with the aid of LC/MS/MS. The composite illustrated reusability and stability without considerable loss in the degradation performance after repeated runs. This work builds on the development of more effective photocatalysts and provides a glimpse into applications for similar MOF heterojunction photocatalysts.

Keywords: photocatalysis; MOF; carbamazepine; pharmaceutical wastewater; anatase TiO_2

Citation: Goh, J.W.; Xiong, Y.; Wu, W.; Huang, Z.; Ong, S.L.; Hu, J.Y. Degradation of Carbamazepine by HF-Free-Synthesized MIL-101(Cr)@Anatase TiO_2 Composite under UV-A Irradiation: Degradation Mechanism, Wastewater Matrix Effect, and Degradation Pathway. *Water* **2022**, *14*, 3964. https://doi.org/10.3390/w14233964

Academic Editor: Christos S. Akratos

Received: 5 November 2022
Accepted: 28 November 2022
Published: 5 December 2022

1. Introduction

Heterogenous photocatalysis to degrade recalcitrant pollutants has been regarded as a promising advanced oxidation process (AOP) for water purification [1]. TiO_2 is one of the most widely used photocatalysts, but it has been plagued by disadvantages such as the rapid recombination of photoelectrons and holes and a broad energy band gap of 3.2 eV. These characteristics restrict its photocatalytic degradation potential. There are generally two approaches to overcome these pitfalls: (1) oxidant coupling and (2) material modification. Oxidant coupling focuses on additive oxidants, such as O_3, Fe^{2+}/Fe^{3+}, H_2O_2, $S_2O_8^{2-}$, and BrO_3^-, which scavenge electrons to generate additional •OH. However, they present challenges, such as the need to consider the removal of residual oxidants, the potential for high operating costs due to the chemical reagents involved, and the need to customise the chemistry to specific pollutants. Another approach is a material modification, which involves coupling with another photocatalyst to form heterojunctions.

Materials of Institute Lavoisier-101 (Cr), MIL-101(Cr), has been widely employed as a co-catalyst to promote kinetic processes such as charge separation or other catalytic reactions [2–8]. By leveraging the potential of MIL-MOFs as new semiconducting photocatalysts [9], the surface of MIL-101(Cr) can be altered by impregnating it with anatase TiO_2. Due to its highly porous structure, MIL-101(Cr) also has the potential for the adsorptive removal of PPCPs, dyes, and N- or S-containing groups [10–18]. Hence, the integration of MIL-101(Cr) and TiO_2 will therefore present three benefits: (1) the porous structure of MIL-101(Cr) can potentially adsorb pollutants rapidly and with better affinity than TiO_2, (2) the photocatalytic efficiency will be enhanced due to delayed photoelectron and hole recombination, and (3) a bifunctional composite will be formed as an adsorbent for the accumulation of pollutants and photocatalysts for degradation.

A chromium terephthalate metal–organic framework, also known as MIL-101(Cr), consists of trimeric chromium (III) octahedral clusters interconnected by 1,4-benzenedicarboxylates, resulting in a highly porous three-dimensional surface. Large pores (29 and 34 Å) and a high BET surface area (>3000 m^2/g) with coordinatively unsaturated open metal sites have attracted considerable interest [19]. It can be synthesised using either the hydrothermal/solvothermal approach or the microwave-assisted method, much like any other MOF. It has been suggested that MIL-101(Cr) crystallises optimally between 200 and 220 °C. It has also been recommended [19] that hydrofluoric acid (HF) be used in the production of MIL-101(Cr) to enhance its crystallinity.

CBZ is an antileptic and anticonvulsant medication. It is known to be recalcitrant and resistant to biological treatment, with less than 10% removal in typical sewage treatment plants (STPs) [20,21]. The toxicity potential cannot be ignored either, with it being classified as a class 1 pharmaceutical on the Global Water Research Coalition's standard list of pharmaceuticals [22]. Pharmaceutical residues such as CBZ have only been commonly reported in sewage effluents and surface waters [23]. They have been attributed to metabolic excretion, improper disposal, and livestock and hospital waste. However, pharmaceutical production plants, which are sources of API pollution, have been constantly overlooked [24]. CBZ is one of the commonly reported APIs in pharmaceutical wastewater effluent [25–28] (Table S1) in the range of mg/L, with them being 500 orders higher than the highest concentration found in STP effluent [25,26,29]. The review also encouraged the evaluation of the photodegradation of such organic contaminants in real wastewater matrices [9]. There is insufficient research on the influence of common wastewater constituents such as Cl^-, SO_4^{2-}, HCO_3^-, CO_3^{2-}, and pharmaceutical organic solvents that may have the capacity to scavenge away ROS species such as •OH.

In this study, for the first time, the degradation of carbamazepine (CBZ) via the UV-A/HF-Free MIL-101(Cr)@TiO_2 process was systematically investigated. Similar MIL-101(Cr)-TiO_2 composites under UV-A irradiation have demonstrated an increased photodegradation efficiency on organic compounds such as methyl orange (MO) and bisphenol A (BPA) [30,31]. Therefore, the effects of the synthesis conditions (TiO_2: MIL-101, calcination temperature), operational parameters (pH, UV intensity, dosage, initial CBZ concentration), and pharmaceutical wastewater matrix on CBZ degradation via the UV-A/MIL-101(Cr)@TiO_2 process were comprehensively studied in this study. CBZ degradation pathways and transformation products are not equivalent in photodegradation methods such as photo-electrolysis, photolysis, and photocatalysis [32]. Therefore, it was also necessary to examine the degradation pathways of CBZ under UV-A/MIL-101(Cr)@TiO_2. Until now, no research has been conducted to determine the ROS responsible for degrading CBZ for UV-A/MIL-101(Cr)@TiO_2. In a similar system such as this, superoxide anion radicals ($O_2^{\bullet -}$) have been found to be the main ROS species that break down BPA using only indirect radical probing methods [31]. In this study, direct and indirect ROS experiments were employed to ascertain the ROS responsible for degrading CBZ. Previous research [30,31] used mineralisers such as hydrofluoric acid (HF) to improve the crystallinity of the MIL-101(Cr) of MIL-101(Cr)@TiO_2 during synthesis. However, the corrosive nature of HF might prevent such composite use. Furthermore, the role of fluoride in the synthesis has not been

well understood in previous studies. This raises the question of whether the mineraliser is crucial to the composite's overall adsorption and photocatalytic performance. Hence, the HF-free synthesised composite was worthy of further investigation.

2. Materials and Methods

2.1. Chemicals and Reagents

The chemicals and reagents used in this study are listed in Text S1.

2.2. Pharmaceutical Wastewater Characterization

Pharmaceutical wastewater samples were obtained from a local pharmaceutical facility in Singapore. They were kept in polyethylene containers at 4 °C. Before characterisation and reaction, the collected materials were filtered via 0.45 µm filters. Two pharmaceutical wastewater samples were collected: PWS 1 and PWS 2. The effluent from these pharmaceutical facilities often changes in composition and concentration. The literature frequently describes pharmaceutical wastewater with elevated COD, TDS, and salinity [33–35]. Both pharmaceutical wastewater samples were characterised by surrogate parameters such as pH, COD, TOC, and total dissolved solids, as seen in Table S2.

2.2.1. Total Alkalinity (as $CaCO_3$)

An alkalinity test was conducted for the wastewater samples using titration methods and the derivation of total alkalinity is shown in Table S3. The presence of alkalinity has been previously reported in pharmaceutical industrial wastewater as well [36].

2.2.2. Inorganic Ions

The samples were placed in 5 mL Thermo Scientific IC vials and measured using a DIONEX ICS-1600 (Thermo Fisher Scientific, MA, USA) equipped with a DIONEX AS-DV (Thermo Scientific, MA, USA) autosampler. Common anions such as Cl^- and SO_4^{2-} have been commonly reported in previous studies [33] and were found in the wastewater samples (PWS 1 and PWS 2) (Table S4).

2.2.3. Pharmaceutical Organic Solvents

Organic solvents are utilized throughout production, and they are primarily responsible for the effluent consisting of highly concentrated wastewater. Some of these pharmaceutical organic solvents used in production have been reported in the literature [33]. With the use of GC/MS, two of the reported organic solvents were identified in PWS 1 and PWS 2: tetrahydrofuran (THF) and N, N dimethyl-formamide (DMF).

Pharmaceutical wastewater samples were injected directly into a GC-2010-QP2010 (Shimadzu, Kyoto, Japan) with an AOC-5000 auto injector. Using a DB1301 column (low to moderate polarity; length (30 cm) × diameter (0.24 mm I.D) × film (0.25 µm)) and a temperature program as seen in Table S5, the non-nitrogenous organic solvent was identified in PWS 1 as tetrahydrofuran, as shown in Figure S1. Using a mega-wax column (high polarity; length (30 cm) × diameter (0.25 mm I.D) × film (0.25 µm)) and with a temperature program as seen in Table S6, the nitrogenous organic solvent was identified in PWS 2 as N, N dimethylformamide (DMF), as shown in Figure S1.

2.3. Synthesis of HF-Free MIL-101(Cr)

Using a mixture of chromium (III) nitrate, H_2BDC, and deionized water in the proportions of 2.0 g, 0.83 g, and 24 mL, respectively, MIL-101(Cr) was hydrothermally synthesised [37]. The solution was properly mixed and sonicated for 30 min before being transferred into a 50 mL Teflon-lined stainless-steel autoclave reactor and heated at 200 °C for 12 h. The crude product was then centrifuged after being rinsed with DI water. To remove any unreacted H_2BDC, 24 mL of DMF was added and the mixture was heated in an autoclave for 12 h at 100 °C. A solvothermal treatment of synthesised MIL-101I was performed using 24 mL of ethanol in an autoclave reactor at 120 °C for 12 h in order to

eliminate any leftover DMF or H_2BDC from the pores of MIL-101(Cr). The product was then vacuum-dried overnight at 150 °C.

2.4. Synthesis of Anatase MIL-101(Cr)@TiO_2 Composite

An amount of 80 mg of MIL-101(Cr) was added to a solution of TBOT (1 mL) and ethanol (32 mL) [30,31]. An amount of 0.8 mL of ultrapure water was added after 30 min of homogeneous mixing by magnetic stirring to ensure suspension uniformity. The suspension was then transferred to an autoclave lined with Teflon and heated to 200 °C for 3 h. The product was then isolated by centrifugation, washed with hot ethanol, and dried for 24 h.

2.5. Material Characterization

A transmission electron microscope (TEM), FEI Talos F200 (Thermo Fisher Scientific, MA, USA), equipped with HRTEM, and EDS mapping were used to examine the catalyst's structures and morphologies. FTIR spectra were determined to identify the chemical features of the catalyst using a Bruker spectrometer (Bruker, MA, USA) with diamond-attenuated total reflectance (ATR). The elemental composition of the catalyst's surface was identified using XPS, Thermo ESCALAB 250XI (Thermo Fisher Scientific, MA, USA). The Raman spectrum of the catalyst was determined with an InVia InSpect confocal Raman microscope (Renishaw, England, UK) using a laser wavelength of 514 nm. The crystalline properties were determined using XRD Bruker D8 Advance (Bruker, MA, USA) with Cu Kα radiation (35 kV, 30 mA). The thermal stability of the material was examined using TGA Q500 (TA Instruments, New Castle, USA) with a platinum weighing pan. The N_2 adsorption–desorption isotherms and BET cumulative specific surface area were determined by NOVA 2200e (Quantachrome, Florida, USA).

2.6. Optical Properties of Material

The fluorescence emission spectrum of the catalyst was determined with a Cary Eclipse fluorescence spectrophotometer (Agilent, California, USA) with an excitation wavelength of 300 nm. A UV-Vis absorbance spectrum was utilized to assess the photocatalyst's optical properties. The spectrum was determined by PerkinElmer Lambda 1050+ UV/VIS/NIR (PerkinElmer, MA, USA). The absorbance spectrum could be fitted into the Tauc plot using Equations (1) and (2) [38]:

$$\alpha\left(\mathrm{cm}^{-1}\right) = 2.302 * \text{Absorbance}\,(\mathrm{au}) \tag{1}$$

$$(\alpha \mathrm{hv})^{1/\gamma} = \mathrm{A}(-\mathrm{v} - \mathrm{E_g}) \tag{2}$$

where α represents the absorption coefficient, h is Plank's constant, v is the photo's frequency, A is the proportionality constant, E_g is the band gap energy, and γ is determined by the type of optical transition of the catalyst. $\gamma = \frac{1}{2}$ and $\gamma = 2$ imply direct and indirect allowed transitions, respectively.

2.7. Adsorption Capability of MIL-101(Cr)@TiO_2 Composite

To investigate the adsorption performances of the composite and virgin MOF, 50 mL of a CBZ aqueous solution (12 mg/L) with a 2 g/L dosage of catalyst was stirred for 30 min; 1.0 mL of the sample was withdrawn at regular intervals using a syringe and filtered with 0.45 µm glass-fibre syringe filters. The concentrations of CBZ were determined by HPLC SPD-10A (Shimadzu, Kyoto, Japan) with acetonitrile/DI (70%v/30%v) at a flow rate of 0.4 mL/min and an Agilent Extend-C18 column (150 mm × 2.1 mm, particle size 5 µm) kept at 40 °C. Figure S2 illustrates the calibration curve of CBZ with detection by HPLC-DAD at a 285 nm wavelength. The adsorption capacity was calculated using Equation (3):

$$q_t = \frac{V(C_o - C)}{m} \tag{3}$$

where C_o is the initial concentration of CBZ, C is the CBZ concentration in the bulk solution at a given time, V indicates the volume of the solution, and m represents the composite mass. Theoretical adsorption kinetic models, such as the pseudo first-order model (Lagergren) and pseudo second-order model (Ho and Mckay), were fitted to the experimental data using a non-linear fitting approach. Through iterative optimization, the parameters could be deduced. The non-linear model fit was accomplished with Origin 2019b.

2.8. Photocatalytic Performance of MIL-101(Cr)@TiO_2 Composite

To assess the photocatalytic degradation efficacy of the composite, an aqueous solution containing 12 mg/L was degraded under UV-A/LED illumination 20 W (Shenzhen Fangpu Optoelectronics Co. Pte Ltd., Shenzhen, China) (Figure S3). Using 25 mL of an aqueous CBZ solution with 2 g/L of photocatalyst, the photocatalytic degradation experiments were conducted. The adsorption equilibrium was reached after 10 min of stirring the suspension in a dark box before the start of illumination. An amount of 1.0 mL of sample was periodically sampled and filtered with a syringe filter. The adsorption of CBZ onto the composite was marginal compared to the photocatalytic degradation of CBZ across the reaction time. Therefore, the Langmuir–Hinshelwood pseudo first-order kinetics model as seen in Equation (4), which is commonly used to explain the reaction kinetics of heterogeneous catalytic processes [39], can be simplified to a pseudo first-order kinetic model as shown in Equation (5):

$$r_O = k_T * \theta = -\frac{dC}{dt} = \frac{k_T * K_{LH} * C_o}{1 + K_{LH} * C_o} \quad (4)$$

where K_{LH} is the Langmuir–Hinshelwood adsorption equilibrium constant (L mg^{-1}) and k_T is the reaction rate constant ($mg.L^{-1}min^{-1}$):

$$\log\left(\frac{C_t}{C_o}\right) = k_{obs}t \quad (5)$$

where t is the reaction time (s), C_o and C_t are the initial concentration and concentration at time t, and k_{Obs} is the observed pseudo first-order rate constant.

2.9. pCBA Radical Probe (•OH)

The steady-state concentration of •OH radicals can be determined using an indirect method involving 4-chlorobenzoic acid (*p*CBA) as a probe compound, detected by HPLC SPD-10A (Shimadzu, Kyoto, Japan) at a wavelength of 236 nm. The rate of degradation of *p*CBA can be expressed in Equation (6):

$$-\frac{dC_{pCBA}}{dt} = K_{\bullet OH,pCBA} C_{pCBA} C_{\bullet OH} \quad (6)$$

where C_{pCBA} is the concentration of *p*CBA and $K_{\bullet OH,pCBA}$ is 5×10^9 M^{-1} s^{-1}.

The integration of the above equation yields Equation (7):

$$\ln \frac{C_{pCBA}}{C_{pCBA_0}} = K_{\bullet OH,pCBA} C_{\bullet OH} t \quad (7)$$

The ln (*p*CBA/[*p*CBA]$_o$) was plotted against reaction time on a graph. The slope of the straight lines was equal to $K_{\bullet OH}$, *p*CBA, and $C_{\bullet OH}$ multiplied together. The rate constant of the reaction between the •OH radicals and *p*CBA was 5×10^9 M^{-1} s^{-1} [40]. With the known value of $K_{\bullet OH,pCBA}$, the pseudo steady-state •OH concentration could be calculated.

2.10. Analytical Methods

The total organic carbon (TOC) of the water samples was measured using a TOC-L analyser (Shimadzu, Kyoto, Japan). Carbamazepine and its intermediates were determined using an LC/MS/MS system 8030 (Shimadzu, Kyoto, Japan) with a simple binary gradient for chromatographic separation and a Shim-pack FC-ODS column (150 × 2 mm, particle size 3 µm) at 40 °C. At a flow rate of 0.25 mL/min, the mobile phase was composed of DI water (A) and methanol (B). An amount of 10 µL of the sample was injected. The concentrations of Cr leeched into the bulk solution were measured by ICP-OES.

3. Results and Discussion

3.1. Material Characterization

The TEM with HTREM and EDS mapping analyses were undertaken to gather additional information on the microstructure of the composite. As seen in Figure 1A, the MIL-101(Cr) surface was coated with TiO_2 nanoparticles, indicating that the composite was successfully synthesised by the solvothermal method as intended. EDS characterisation verified the presence of the Ti, Cr, and O elements, with the EDS mapping pictures (Figure 1D–F) displaying the distribution of each element and point detection (Figure 1C), indicating the possible weight % and atomic % of MIL-101(Cr)@TiO_2 as seen in Table S7. Figure 1E, which depicts the organic structure, reveals that Cr was encased within the composite. It could also be verified that the attachment of TiO_2 nanoparticles does not significantly alter the surface morphology of MIL-101(Cr).

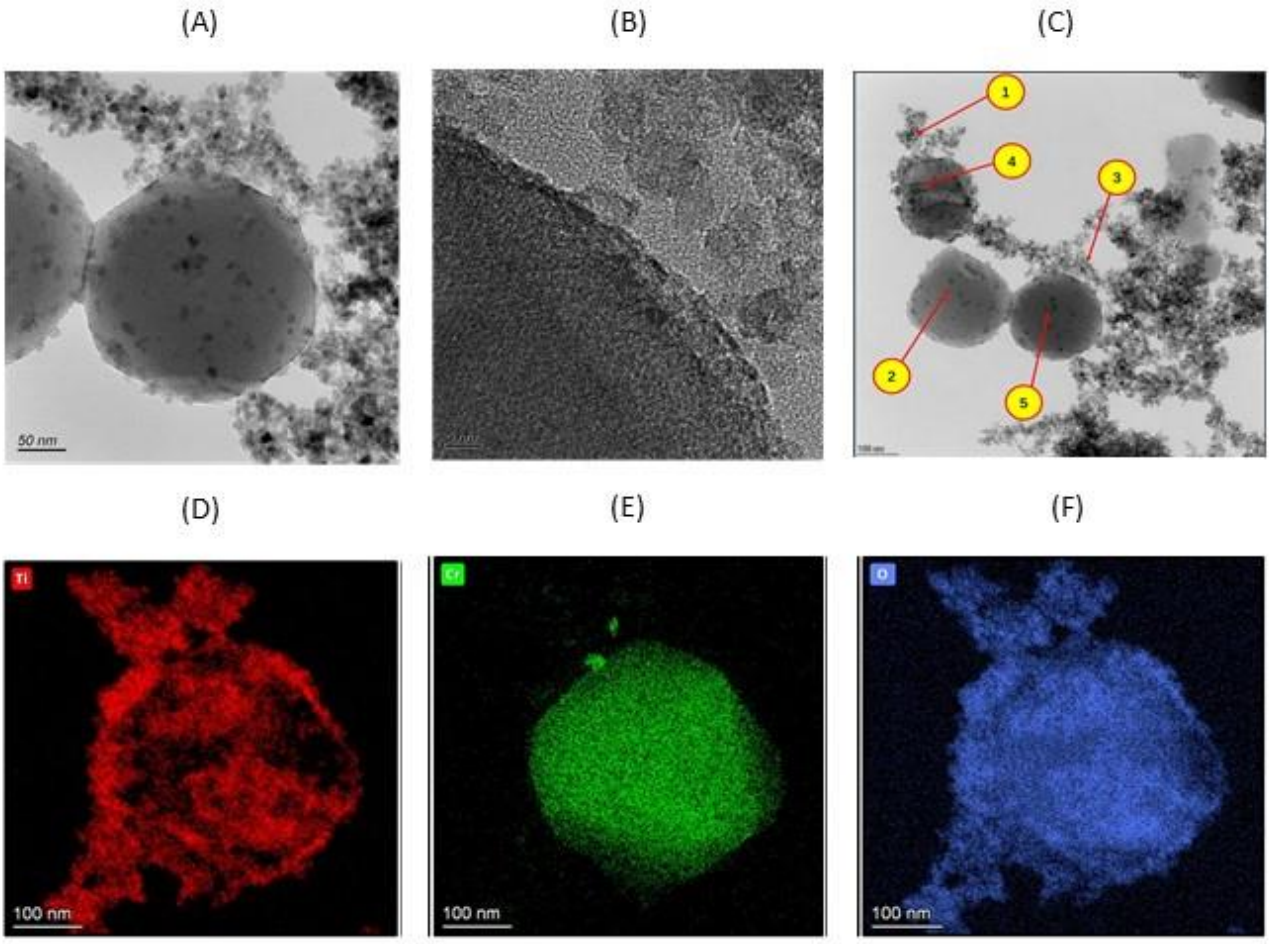

Figure 1. (**A**) Transmission electron microscopy (TEM); (**B**) high-resolution transmission electron microscopy (HRTEM); (**C**) transmission electron microscopy energy-dispersive spectroscopy (TEM EDS) point detection, EDS mapping; and the (**D**) Ti, (**E**) Cr, and (**F**) O of the MIL-101(Cr)@TiO_2 composite.

As demonstrated in Figure 2A, the FTIR spectra of MIL-101(Cr) were comparable to those of other studies, with the collective identification of symmetric (O-C-O) vibrations of dicarboxylate at 1397 cm^{-1} [41–43]. The asymmetric stretching of C=O vibrations supported the presence of dicarboxylate at 1509.24 cm^{-1} [42]. The benzene ring was observed between 700 and 1700 cm^{-1}, with a prominent peak indicating a stretching vibration (C=C) at 1625 cm^{-1} [42]. Weak and narrow peaks at the wavenumbers 714.73 cm^{-1}, 832.29 cm^{-1}, and 1055.53 cm^{-1} indicated that the benzene ring's deformed vibration (C-H) was present [42]. It was also evident that the C=O stretching bond at 1625 cm^{-1} in MIL-MOFs' spectra was greatly diminished compared to its reactant, H_2BDC, indicating effective synthesis. As shown in Figure 2B, the FTIR spectrum of MIL-101(Cr)@TiO_2 was an amalgamation of the respective spectra of MIL-101(Cr) and TiO_2. As shown in Figure 2C, the XRD spectrum of MIL-101(Cr) corresponded to the simulated XRD spectra produced from the crystallography database, with diffraction peaks found at 8.5° and 9° [44]. Figure 2D illustrates the incorporation of anatase TiO_2 into the composite at 2θ = 25.43°, 37.92°, 48.09°, 54.58°, 62.81°, and 78.89° [45]. As demonstrated in Figure 2E, the vibrational bands of the MIL-101(Cr) Raman spectrum emerged at 1618 cm^{-1}, 1461 cm^{-1}, 1149 cm^{-1}, and 873 cm^{-1}, confirming the presence of aromatic and dicarboxylate groups in H_2BDC, and the spectrum was comparable to those of earlier research [46,47]. As depicted in Figure 2F, the Raman spectrum of anatase TiO_2 comprised six vibrational modes: 143 cm^{-1}, 195 cm^{-1}, 396 cm^{-1}, 518 cm^{-1}, and 639 cm^{-1}. These modes were visible in both the TiO_2 and MIL-101(Cr)@TiO_2 spectra. MIL-101(Cr) was responsible for the extra peak at 1618 cm^{-1} for MIL-101(Cr)@TiO_2. However, MIL-101(Cr) was significantly less intense than TiO_2.

As seen in Figures S4–S7, the XPS spectra were used to analyse the surface characteristics and valance states of the MIL-101(Cr)@TiO_2 surface components. The high-resolution spectra of Ti2p (Figure S4) revealed two peaks at 458.52 and 464.22 eV, which corresponded to Ti $2p_{3/2}$ and Ti $2p_{1/2}$, previously observed in comparable MIL-101(Cr)@TiO_2 composites [48,49]. Two peaks at 530 eV and 531 eV were observed in the O1s spectrum (Figure S5), which were attributed to the Ti-O-Ti and Ti-O-H bonds of TiO_2. The two peaks at 587.2 and 577.6 eV in Figure S6 corresponded to Cr $2p_{1/2}$ and Cr $2p_{3/2}$, respectively [50,51]. Comparing the spectra to the database yielded identical responses stated in the literature to Cr (III) oxide (Table S8), indicating the presence of Cr^{3+}. Similar to the literature, a peak at 533.5 eV in Figure S7 was owing to the presence of a C-O bond, indicating that MIL-101(Cr)@TiO_2 has a heterostructure [31].

3.2. Adsorption Affinity of CBZ onto MIL-101(Cr)

The adsorption affinity between virgin MIL-101(Cr) and CBZ was established earlier with experimental data being fitted to both adsorption isotherm and kinetic models (Figure S8). The Freundlich model best described the adsorption of MIL-101(Cr) (Table S9), as MOFs such as MIL-101(Cr) are known to have diverse heterostructures. The values of the isotherm and kinetic models were in the same order of magnitude as those previously published [18], indicating a consistent adsorption relationship between CBZ and HF-free synthesized MIL-101(Cr). Furthermore, the K_L calculated based on a Langmuir isotherm of 0.73 and 1/n from a Freundlich isotherm of 0.83 indicated that the CBZ adsorption with MIL-101(Cr) was favourable.

The N_2 adsorption–desorption isotherm (Figure 3B) corresponded to the Type I IUPAC isotherm, as reported in the literature [19,31,52]. This shows that the structure is predominantly microporous (<2 nm). However, it is important to note that the BET surface area and pore volume of MIL-101(Cr) in this study were 682.204 m^2/g and 0.493 cm^3/g, and they were significantly lower than those often reported in the literature [31,52,53]. This can be attributed to the absence of HF mineraliser.

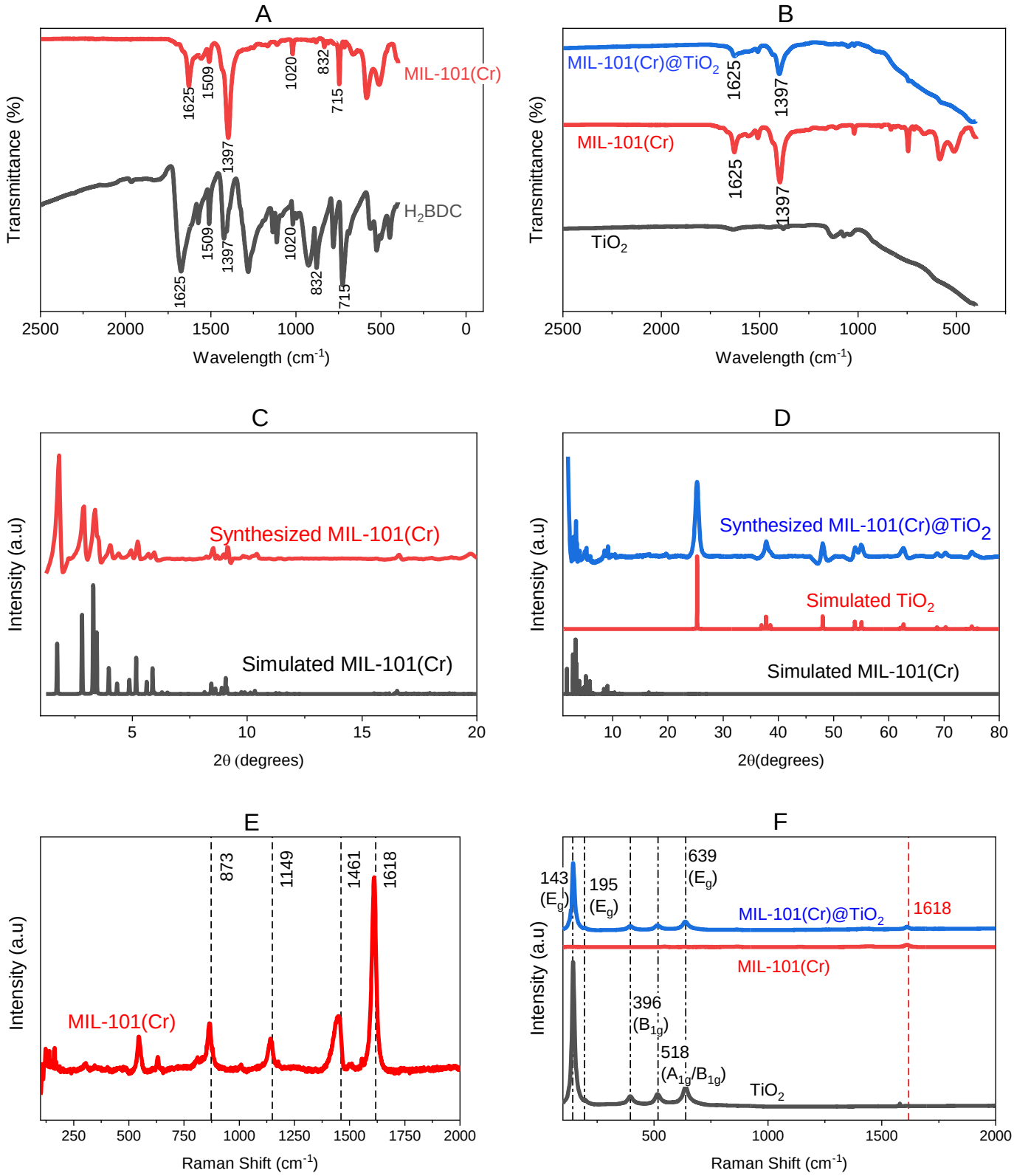

Figure 2. FTIR spectra of (**A**) H_2BDC and MIL−101(Cr), and (**B**) MIL−101(Cr)@TiO_2, MIL−101(Cr), and TiO_2; XRD spectra of (**C**) synthesised and simulated MIL−101(Cr), and (**D**) synthesised MIL−101(Cr)@TiO_2 and respective simulated constituents; Raman spectroscopy of (**E**) MIL−101(Cr), and (**F**) MIL−101(Cr)@TiO_2 and TiO_2.

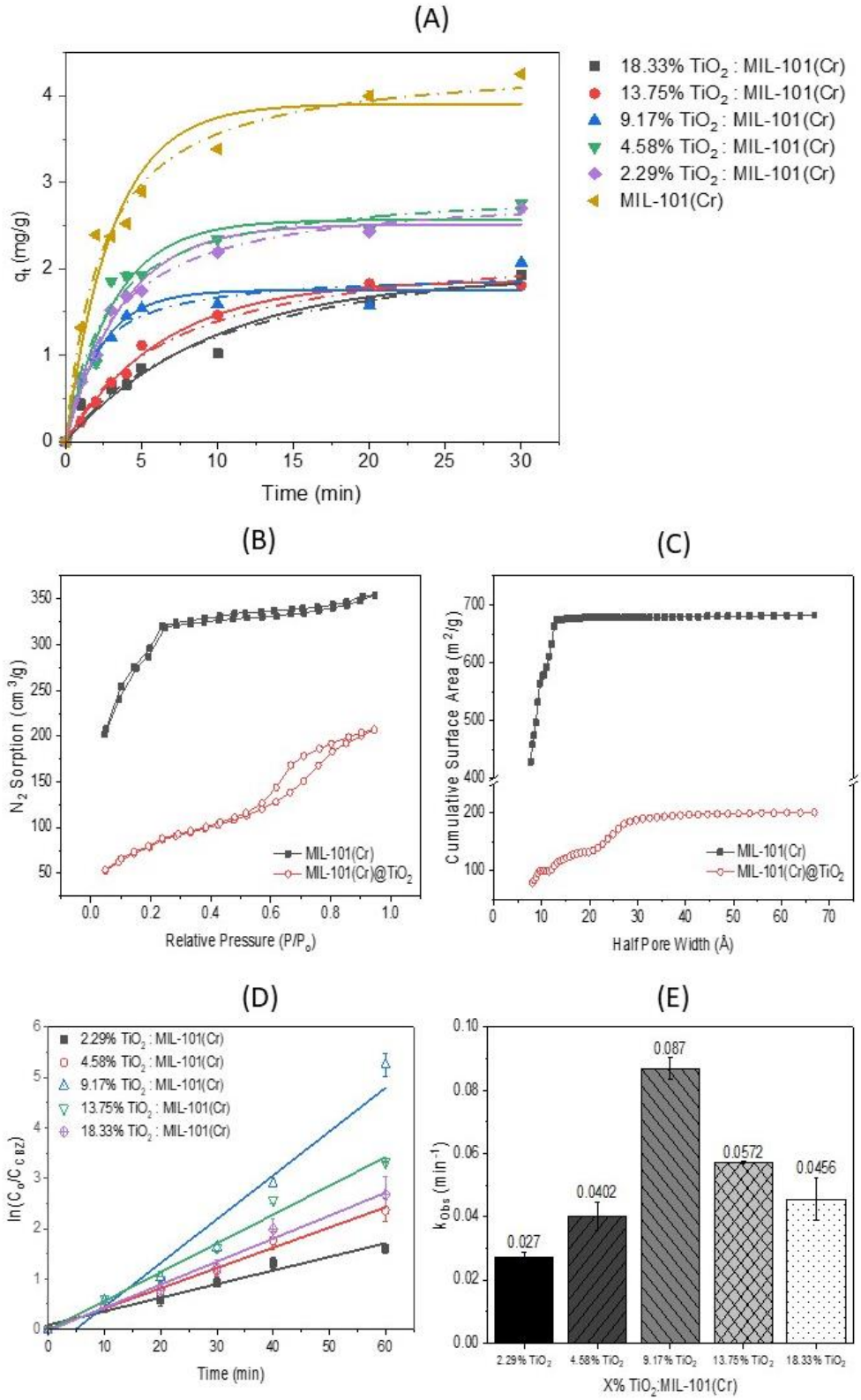

Figure 3. (**A**) Adsorption kinetics models (Pseudo 1st and 2nd) for varied percentages of TiO_2: MIL-101(Cr) composite; (**B**) N_2 adsorption–desorption isotherms; (**C**) BET cumulative specific surface area of MIL-101(Cr) and 9.17% MIL-101(Cr)@TiO_2 composite; (**D**) $\ln(C_o/C_{CBZ})$ against time; and (**E**) k_{Obs}, min^{-1} for varied MIL-101(Cr): TiO_2 ratio composites.

3.3. Optimal Synthesis Condition

3.3.1. Varied TiO_2:MIL-101(Cr) Ratio

The adsorption capacity and photocatalytic degradation capabilities of varied TiO_2:MIL-101(Cr) composites for CBZ were investigated. As seen in Figure 3A, the experimental data were fitted into both the pseudo first- and second-order adsorption kinetic models (Lagergren, and Ho and Mckay) as seen in Table S10. It was observed that an increase in TiO_2 resulted in a lower adsorption equilibrium (mg/g). The adsorption equilibrium (q_e) of virgin MIL-101(Cr) decreased from 4.424 mg/g to 1.965 mg/g for the 9.17% TiO_2:MIL-101(Cr) composite when fitted to the pseudo second-order adsorption kinetic. This is consistent with studies indicating that TiO_2 obstructs absorption sites between the adsorbate and adsorbent for π–π interactions [31], which is the dominant adsorption mechanism between MIL-101(Cr) and CBZ [18].

Figure 3B,C further demonstrates that TiO_2 obstructed the adsorption sites, as the size of the N_2 adsorption–desorption isotherm and the BET surface area were decreased. The BET surface area and pore volume of the 9.17% MIL-101(Cr)@TiO_2 composite were 200.209 m^2/g and 0.297 cm^3/g, respectively. As displayed in Figure 3B, a type IV isotherm with a hysteresis loop was observed, which was attributed to the greater presence of mesopore structures in MIL-101(Cr). This is consistent with the literature for similar composite synthesised [31].

However, the addition of TiO_2 somehow increased the effectiveness of the photocatalytic degradation. The TiO_2 percentage affected the degradation efficiency of CBZ, with 9.17% TiO_2:MIL-101(Cr) demonstrating greater photodegradation of CBZ than 4.58% TiO_2:MIL-101(Cr), although the adsorption capacity was the opposite.

Overall, the adsorption and degradation capabilities continued to decrease as the TiO_2 level increased. The fall in the photocatalytic degradation of CBZ when the ratio of TiO_2 to MIL-101(Cr) was more than 9.17% could be attributed to light scattering caused by an increase in the TiO_2 content, which hindered the photons received and decreased the apparent reaction rate [54,55]. Similar to the CBZ degradation trend, $[\bullet OH]_{ss}$ peaked at a 9.17% TiO_2:MIL-101(Cr) ratio over a range of TiO_2:MIL-101(Cr) ratios (Table S11).

3.3.2. Calcination Temperature

Due to the recognized constraint of low stability at high temperatures for MOFs such as MIL-101(Cr), the calcination of the composite material was studied [56]. The assessed calcination temperature range was between 100 °C and 400 °C. As shown in Figure 4A,B, the apparent reaction rate of the CBZ degradation was reduced by 50% at 200 °C and 300 °C due to the disintegration of the organic structure at temperatures >100 °C. This is explained by the TGA curve of MIL-101(Cr) (Figure 4C), which exhibits an apparent weight loss at temperatures above 200 °C, as demonstrated by the peaks of the weight derivative (%/°C) plot.

According to the literature [19,57], the skeleton of MIL-101(Cr) collapses between 200 °C and 300 °C. This may cause the release of one of the key components of MIL-101(Cr), terephthalic acid (TA), which reacts well with •OH radicals. TA is one of the common probes for •OH, along with pCBA, DMPO, coumarin, and luminol [58] (Table S12). Consequently, TA will likely interfere with the degradation of CBZ when the organic framework disintegrates as the temperature rises. The small improvement in CBZ degradation at 400 °C could be due to the complete decomposition of leached TA by thermal heat, resulting in less TA to quench the •OH produced. As shown in Figure S9, the concentration of Cr increased significantly at 400 °C compared to other activation temperatures. As depicted in Figure 4D, photodegradation continued because TiO_2 has great thermal stability, without considerable weight loss even at high temperatures of 900 °C. Consequently, the best calcination temperature for MIL-101(Cr)@TiO_2 was determined to be 100 °C, which is comparable to the results of a separate study [57] that indicated the optimal activation temperature of the adsorbent to be 130–150 °C.

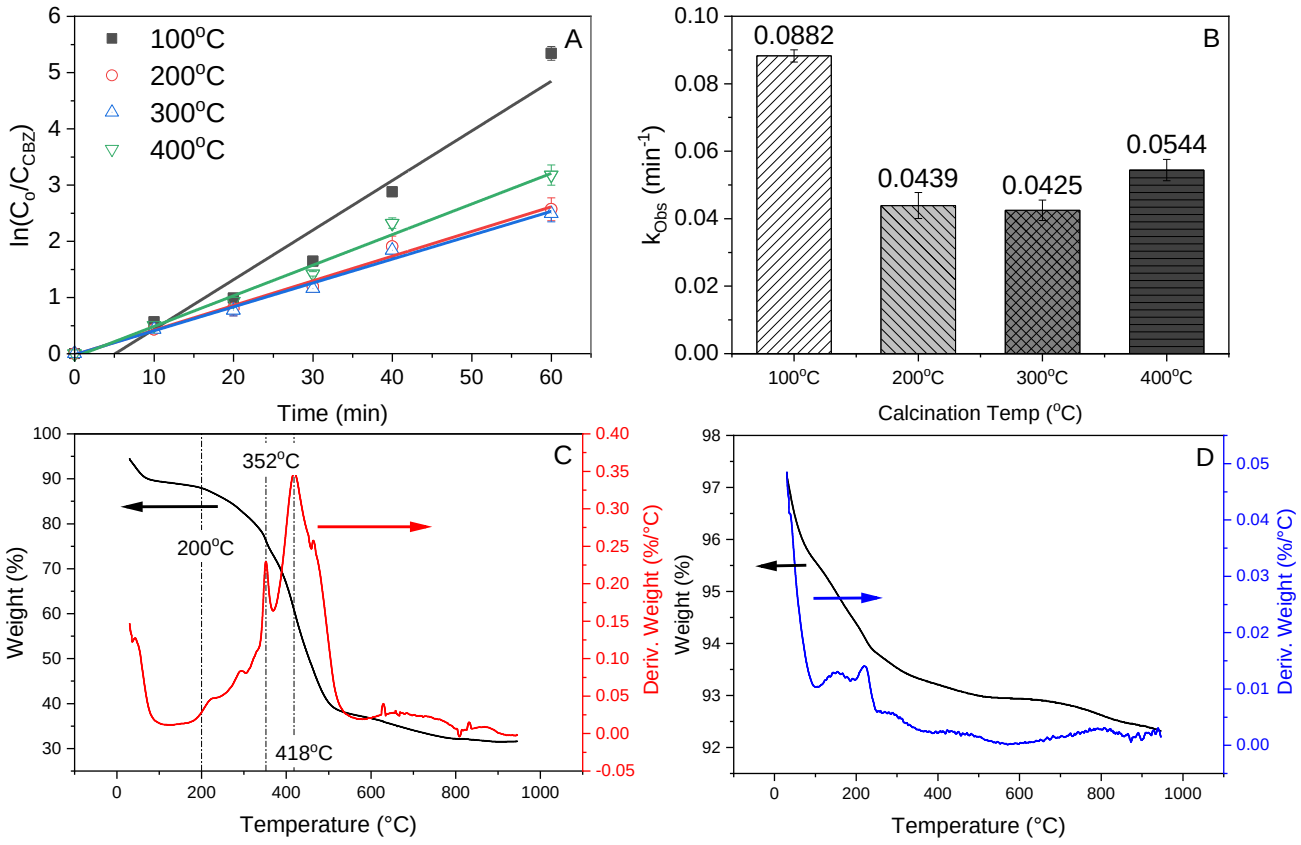

Figure 4. (**A**) ln(C_o/C_{CBZ}) against time at varied temperatures; (**B**) k_{Obs}, min^{-1} due to varied calcination temperatures. TGA curves of (**C**) MIL−101(Cr) and (**D**) anatase TiO_2 under inert conditions (N_2).

3.4. Enhanced Photocatalytic Degradation

As illustrated in Figure 5, the photocatalytic degradation of CBZ using TiO_2 and 9.17% MIL-101(Cr)@TiO_2 were assessed alongside the adsorption capacities of TiO_2, MIL-101(Cr), and 9.17% MIL-101(Cr)@TiO_2. Compared to 84.2 ± 5.4% of TiO_2, the 9.17% MIL-101(Cr)@TiO_2 displayed a greater photocatalytic degradation efficiency for CBZ, at 99% after 60 min (Figure 6A). This was due to the heterostructure of MIL-101(Cr)@TiO_2, which delayed the rapid recombination of the photogenerated h^+ and e^-, hence enhancing the photocatalytic efficiency. As indicated by the Tauc plot (Figure 6C), the decrease in the band gap energy from 3.2 eV (TiO_2) to 2.9 eV was another reason for the enhancement of the photocatalytic performance. The UV absorbance spectra used to generate the Tauc plot (Figure 6C) can be seen in Figure S10.

The fluorescence emission spectrum further illustrated this delay in recombination (Figure 6D). This spectrum can be used to determine the efficiency of charge carrier trapping and to analyse the e^-/h^+ pair in greater detail [59,60]. This electron pair's recombination will result in the emission of fluorescence. Figure 6D demonstrated that with an excitation wavelength of 300 nm, both peaks of the fluorescence emission spectrum occurred at 380 nm. However, the fluorescence intensity decreased due to the introduction of MIL-101(Cr), indicating that the recombination of electrons and holes was delayed. As shown in Figure 6B, the TOC measurement suggested that CBZ could be mineralized by the composite with a degradation efficiency of 80% after 60 min of reaction time.

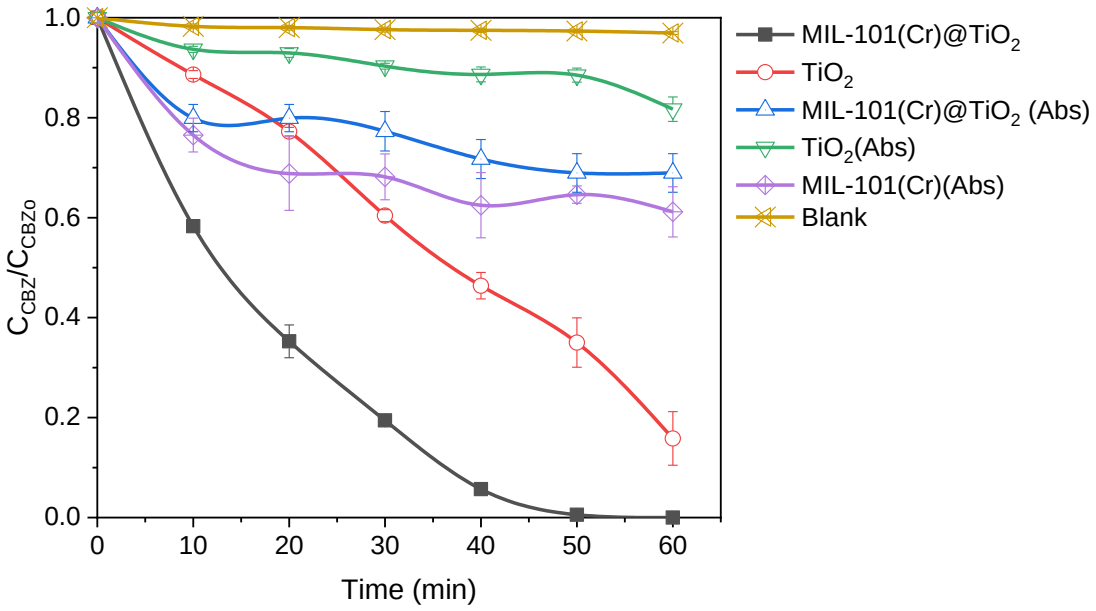

Figure 5. CBZ photocatalytic degradation and adsorption of different samples (2 g/L dosage, 12 mg/L of CBZ, and UV-A irradiation at 35–38 mW/cm^2 with a reaction time of 60 min).

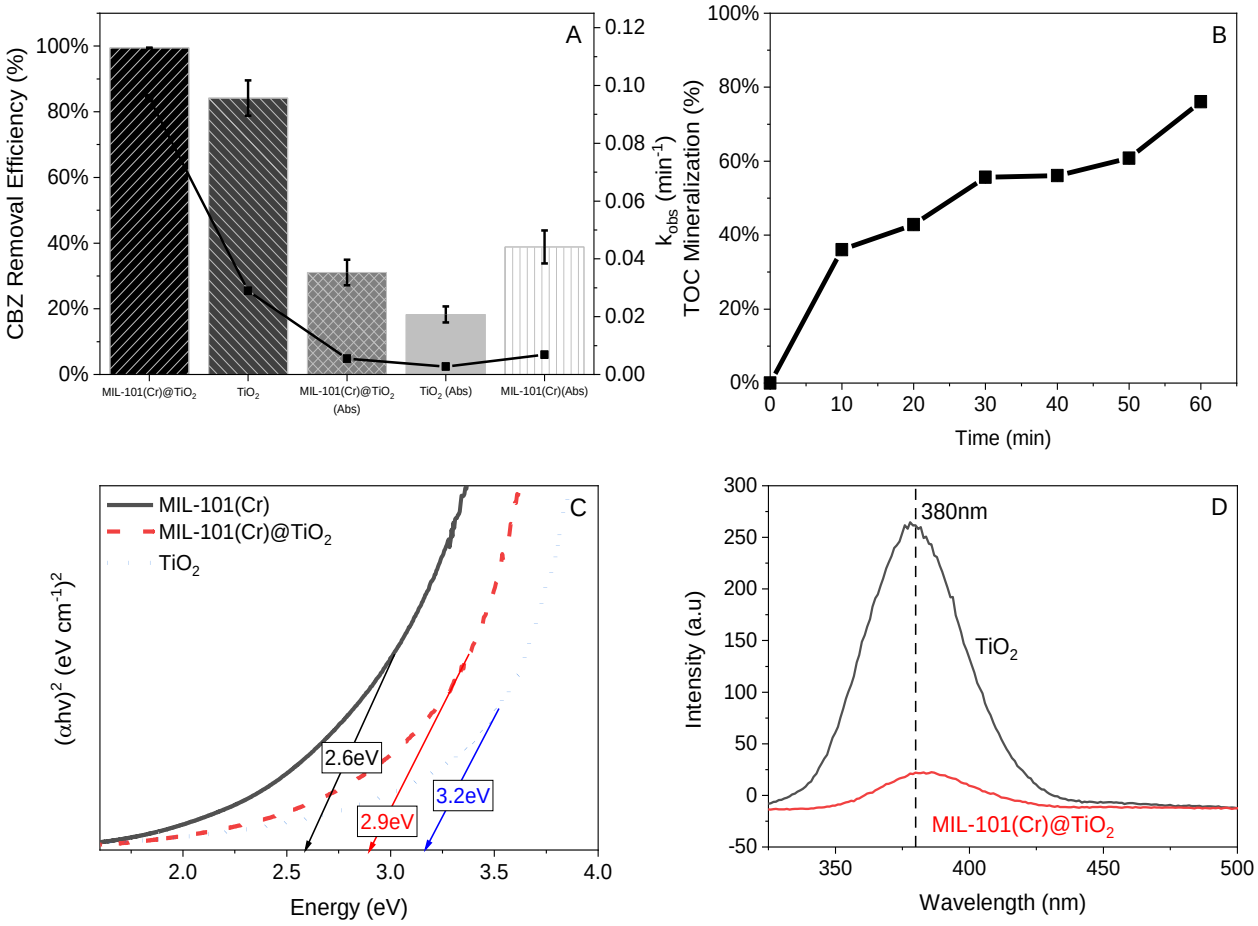

Figure 6. (**A**) CBZ removal efficiency and rate constants of CBZ degradation (min^{-1}) for various different samples; (**B**) TOC mineralization (%) of CBZ using UV−A/MIL−101(Cr)@TiO_2; (**C**) Tauc plot of MIL−101(Cr), MIL−101(Cr)@TiO_2, and TiO_2; and (**D**) fluorescence emission spectrum of MIL−101(Cr)@TiO_2 and TiO_2.

3.5. Proposed Mechanism of UV-A/MIL-101(Cr)@TiO_2

The suggested reaction mechanism in this photocatalytic system was supported by the photocatalyst's conduction band (E_{cb}) and valence band (E_{vb}) potentials. These can be determined with Equations (8) and (9) using the Mulligan function of electronegativity:

$$E_{vb} = X - E^e + 0.5E_g \quad (8)$$

$$E_{cb} = E_{vb} - E_g \quad (9)$$

where X is the predicted electronegativity of the material, E^e is the energy of a free electron on the normal hydrogen electrode (NHE) scale (4.5 eV), and E_g is the band energy gap. The literature proposes and calculates the E_{cb} and E_{vb} to be −1.57 eV and +0.49 eV, with the latter being the redox potential of Cr^{3+}/Cr^{2+} [4,61–63]. X is the geometric mean of the individual element electronegativity values (eV) and can be calculated using Equation (10):

$$X(A_\alpha B_\beta C_\gamma) = \sqrt[\alpha+\beta+\gamma]{X_{A_\alpha} X_{B_\beta} X_{C_\gamma}} \quad (10)$$

Consequently, $X(TiO_2)$ was calculated to be 5.309 eV using published estimates [64] and Equation (10). Using Equations (8) and (9), the E_{vb} and E_{cb} were calculated to be 2.409 eV and −0.79 eV, respectively, with the E_g of anatase TiO_2 known to be 3.2 eV. The calculated values are comparable to those published in the cited literature [65,66].

The computed E_{cb} and E_{vb} for both TiO_2 and MIL-101(Cr) indicated that the profile (Figure 7) has a type-II heterojunction structure, which is distinguished by a staggering gap between the two materials. Since the CB of MIL-101(Cr) is more negative than that of TiO_2 (−0.79 eV), electrons are transferred to the CB of TiO_2. Since the VB of MIL-101(Cr) is less positive than that of TiO_2, the photogenerated holes will be moved from the VB of TiO_2 (+2.41 eV) to the VB of MIL-101(Cr) (+0.49 eV). It was hypothesized that these charge transfers inhibit the quick recombination of photoexcited e^- and h^+ pairs, hence enhancing the photocatalytic efficiency. The E_{cb} of both MIL-101(Cr) and TiO_2 was more negative than that of $O_2/O_2^{\bullet-}$ (E_o = −0.33 V vs. NHE); therefore, it is probable that the electrons reacted with O_2 to generate $O_2^{\bullet-}$. Both materials have been reported to be able to have photogenerated electrons stored in their CB [31,62,63] to form $O_2^{\bullet-}$. The energy of TiO_2's h^+ is greater than the potential of -OH/•OH (E_o = 1.99 V vs. NHE). Consequently, photogenerated holes may react with -OH to create •OH.

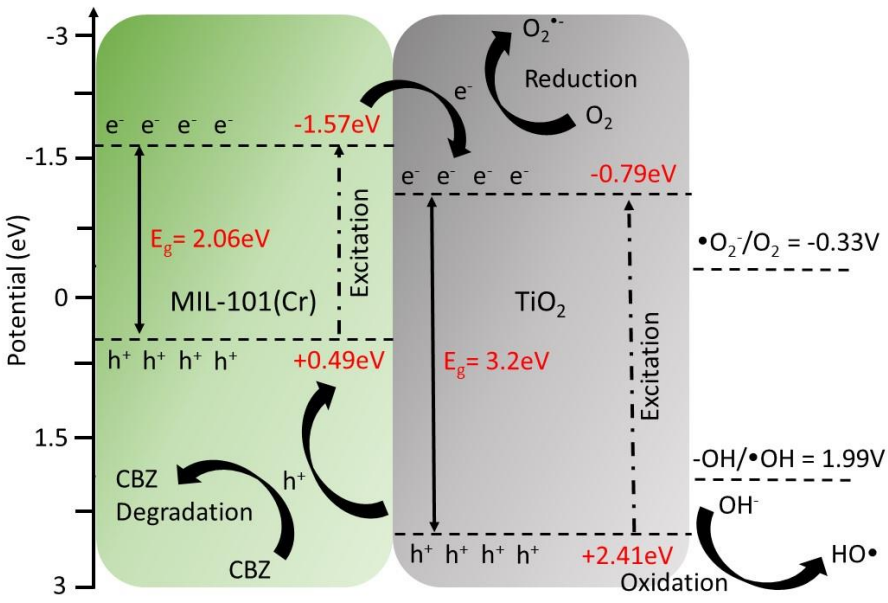

Figure 7. Proposed degradation mechanism using the UV−A/MIL−101(Cr)@TiO_2 system.

3.6. Identification of Main Reactive Oxidants

Oxygen-reactive species were identified using both indirect and probing techniques in an effort to better establish the aforementioned mechanism and identify the major reactive species.

For indirect probing, tert-butanol, potassium iodide (KI), *p*-Benzoquinone (BQ), sodium azide (NaN_3), and silver nitrate ($AgNO_3$) at 1 mM were utilized to quench the radical species •OH, h^+, $O_2^{\bullet-}$, $^1O_2$, and e^-, respectively. As indicated in Figure 8A–D, the photodegradation rate was 0.097 min^{-1} and the CBZ removal efficiency was 99.46% (50 min) in the absence of any free radical quenching agents. NaN_3 had no significant effect on the lowering of the photocatalytic degradation of the composite. With the addition of tert-butanol, KI, and $AgNO_3$, the CBZ degradation rate was reduced from 0.097 min^{-1} to 0.043 min^{-1}, 0.026 min^{-1}, and 0.018 min^{-1}, respectively. The addition of BQ drastically decreased the efficiency of degradation, with the rate of degradation decreasing to 0.0083 min^{-1} and the CBZ removal efficiency decreasing to 36.04% (50 min). This strongly suggests that $O_2^{\bullet-}$ is the predominant oxygen species in the degradation of CBZ by MIL-101(Cr)@TiO_2. This is consistent with prior research [31]. This is in contrast to experiments utilizing TiO_2, where •OH and h^+ are the primary active species for CBZ photodegradation [67].

ESR spectroscopy was used for direct probing to validate the existence of reactive species. As it can create powerful paramagnetic spin-adducts, DMPO was utilized as a spinning-trap agent. The results of its interaction with •OH and $O_2^{\bullet-}$ were DMPO-OH and DMPO-OOH, respectively. The generation of DMPO-OH from •OH and DMPO can be seen in Equation (11):

$$\text{DMPO} + \bullet\text{OH} \rightarrow \text{DMPO-OH} \quad (11)$$

$O_2^{\bullet-}$ can be investigated using the ESR/DMPO spin-trapping approach in an ethanolic solution because the rapid disproportionation of superoxide radicals in water [68] inhibits the slow reaction between $O_2^{\bullet-}$ or $HO_2^{\bullet}$ and DMPO (k = 10 and 6.6 × 10^3 $M^{-1}s^{-1}$, respectively) [69]. As seen from Figure 8E–8F, ESR spectroscopy detected the formation of superoxide anion radicals ($O_2^{\bullet-}$) and hydroxyl radicals (•OH) in the MIL-101(Cr)@TiO_2 system under UV-A irradiation. Due to the distinct ESR splitting patterns, radicals could be identified [69]. Figure 8E depicts the representative 1:2:2:1 quartet signal of DMPO-OH in the DI medium [70]. As demonstrated in Figure 8F, the ESR signal of DMPO-OOH exhibited a similar signature to those reported in the literature [71]. Therefore, the UV-A/MIL-101(Cr)@TiO_2 system generated three primary reactive oxygen species, •OH, $O_2^{\bullet-}$, and h^+, with varying degrees of contribution to CBZ degradation.

3.7. Effects of Operational Parameters

3.7.1. Varied pH Conditions

pH is one of the crucial and prevalent parameters that might influence the decomposition of organic molecules in photocatalytic processes. pH influences the adsorption capacity via adsorbate dissociation, the photocatalyst surface charge, and the valence band oxidation potential [72]. To examine the influence of pH on the CBZ degradation rate, the pH of the CBZ solution (3.0–11.0 pH) was altered with 0.01 M NaOH and 0.01 M H_2SO_4. The maximum degradation rate was 0.157 min^{-1} at a pH of 11 and the minimum degradation rate was 0.0768 min^{-1} at a pH of 3. The CBZ decomposition via a radical-induced reaction was not significantly influenced when the pH was altered between 3.0 and 7.0 (Figure 9A), which is remarkably similar to previous work [73]. The degradation was impacted by pH in the alkaline region (7.0–11.0 pH) (Figure 9A), yielding similar results to a study that utilized TiO_2 photocatalysts [74]. Equation (12) demonstrates that, in the alkaline region, the OH^- enhanced the generation of •OH through photo-oxidation by h_{vb}^+. This has been documented previously [75]:

$$h_{VB}^+ + OH^- \rightarrow HO\bullet \quad (12)$$

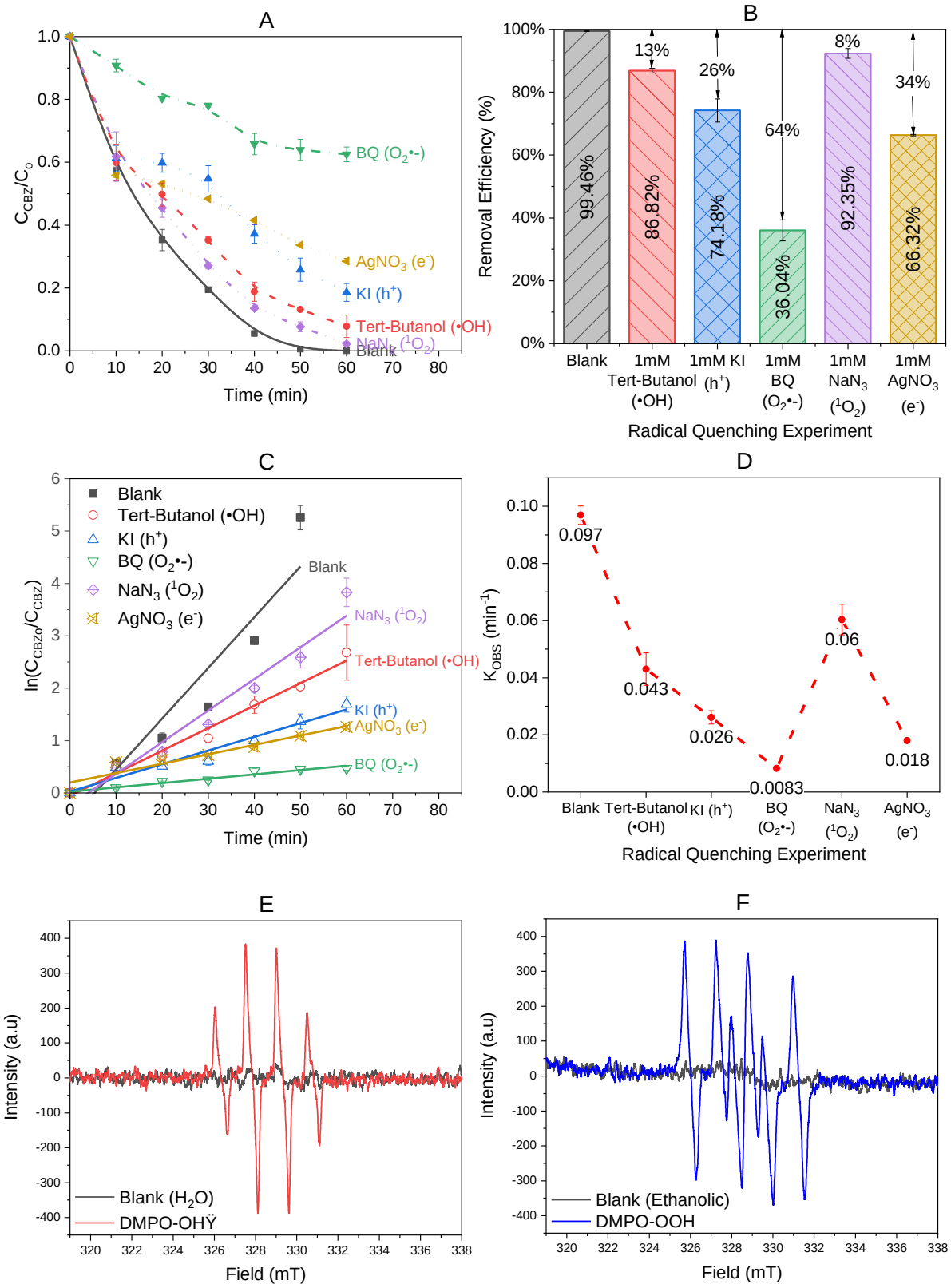

Figure 8. (**A**) C_{CBZ}/C_{CBZo} against time; (**B**) removal efficiency of CBZ (%) at 50 min; (**C**) $\ln(C_{CBZo}/C_{CBZ})$ against time; (**D**) degradation rate constants, min^{-1} due to the effects of different scavengers (MIL−101(Cr)@TiO_2 composite = 2 g/L, CBZ = 10 ppm, UV−A intensity = 36.6 mW/cm^2); and ESR spectra of (**E**) DMPO−OH against dark state and (**F**) DMPO−OOH against dark state (DMPO = 100 mM, MIL−101(Cr)@TiO_2 = 2 g/L).

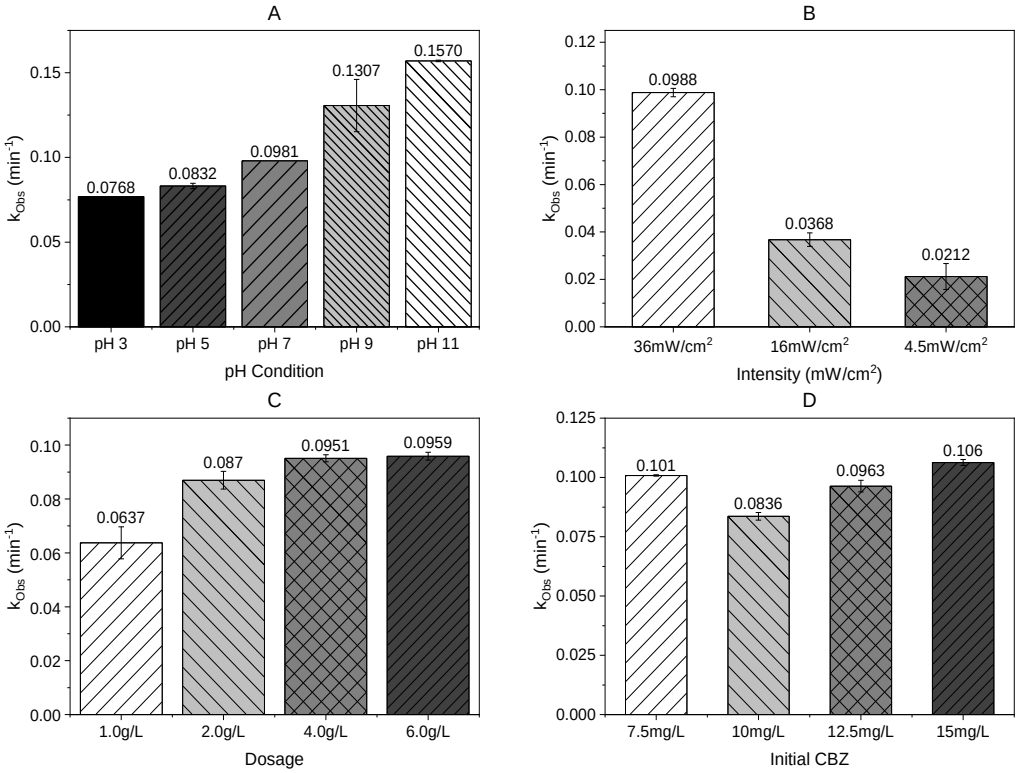

Figure 9. The k_{Obs}, min^{-1} due to (**A**) varied pH conditions, (**B**) varied UV intensities, (**C**) varied dosages of composite, and (**D**) varied CBZ concentrations.

3.7.2. Varied UV Intensity

Light intensity is a crucial photodegradation parameter. The photodegradation rate is proportional to the incident radiant flux [76,77]. The photocatalytic reaction is affected by the electro-hole pairs as a result of the light intensity. An increase in the intensity enhances the excitation of the catalyst. The light intensity can be assessed by altering the distance between the UV-A LED and the solution's surface in order to control the incident photon flux. The distances were 14, 23, and 32 cm, resulting in UV intensities of 36 mW/cm^2, 16 mW/cm^2, and 4.5 mW/cm^2, respectively. Figure 9B demonstrates that the light intensity (mW/cm^2) had a considerable and critical influence, with k_{Obs} being 0.0988 min^{-1}, 0.0368 min^{-1}, and 0.0212 min^{-1} for 36 mW/cm^2, 16 mW/cm^2, and 4.5 mW/cm^2, respectively.

3.7.3. Varied Dosage of Composite

In the photocatalytic degradation process, the catalyst dose is also a crucial element. The effect of the MIL-101(Cr)@TiO_2 dose (g/L) on the kinetics of photocatalytic CBZ degradation was investigated. From 1.0 g/L to 6.0 g/L, the apparent first-order oxidation rate constants were measured for various composite dosages. As seen in Figure 9C, the apparent reaction rate of CBZ degradation increased as the composite dosage increased. The k_{Obs} for the 1.0 g/L, 2.0 g/L, 4.0 g/L, and 6.0 g/L dosages of composite was 0.0637 min^{-1}, 0.087 min^{-1}, 0.0951 min^{-1}, and 0.0959 min^{-1}, respectively. The dosage of the composite had a substantial effect on the degradation kinetics.

3.7.4. Varied Initial CBZ Concentration

Pollutant concentration is another crucial operational parameter that might influence photocatalytic efficiency. According to a prior study, an increase in the concentration of a given organic pollutant is likely to prolong the time required for its complete elimination or degradation [72,76]. This is attributed to the TiO_2 surface being occupied by the pollutants, resulting in drastically diminished adsorptive and photocatalytic capabilities [54,75].

Several studies have shown similar patterns and have attributed the decrease in degradation rate to an insufficient production of •OH during photocatalytic activities [78]. Figure 9D reveals, however, that the initial concentration of CBZ had no significant effect on the apparent reaction rate of CBZ degradation with MIL-101(Cr)@TiO_2. This can be ascribed to the difference in adsorption capacity between the composite and TiO_2, or the fact that $O_2^{\bullet-}$ is the predominant ROS; thus, there is a diminishing influence of the initial concentration on the degradation efficiency of CBZ when •OH does not play a significant role.

3.8. Effects of Inorganic Anions

3.8.1. Bicarbonate (HCO_3^-) Ion

As shown in Figure 10A,B, the addition of HCO_3^- lowered the rate of CBZ degradation by ~16%, ~27%, ~29%, and ~59% for concentrations of 5 mM, 10 mM, 15 mM, and 30 mM HCO_3^-, respectively. The decrease in k_{Obs} was proportional to the [HCO_3^-] concentration. This is demonstrated in Equation (13) (k = (1–2) × 10^6 M^{-1} s^{-1}) [79] and Equation (14) (k = 8.5 × 10^6 M^{-1} s^{-1}) [80], respectively:

$$HCO_3^- + O_2^{\bullet-} \rightarrow HO_2^- + CO_3^{\bullet-} \quad (13)$$

$$\bullet OH + HCO_3^{2-} \rightarrow H_2O + CO_3^{\bullet-} \quad (14)$$

The reaction of HCO_3^- with ROS yielded CO_3^-, which is less reactive with CBZ (k = (2.3–4.2) × 10^6 M^{-1} s^{-1}) than the ROS in the system (k > 10^9) [81].

3.8.2. Carbonate (CO_3^{2-}) Ion

As demonstrated in Figure 10C,D, the presence of CO_3^{2-} slowed the rate of CBZ degradation. The k_{Obs} fell by ~16%, ~56%, ~73%, ~81%, and ~79% when CO_3^{2-} was added at concentrations of 2.5 mM, 5 mM, 10 mM, 15 mM, and 30 mM, respectively. This is demonstrated in Equation (15) (k = (1–2) × 10^6 M^{-1} s^{-1}) [79] and Equation (16) (k = 3.9 × 10^8 M^{-1} s^{-1}) [80]:

$$CO_3^- + HO_2^{\bullet-} \rightarrow HO_2^- + CO_3^{\bullet-} \quad (15)$$

$$\bullet OH + CO_3^{2-} \rightarrow OH^- + CO_3^{\bullet-} \quad (16)$$

As seen in Figure 10A–D, CO_3^{2-} had a greater inhibitory impact than HCO_3^-, with the k_{Obs} decreasing by 73% for 10 mM of CO_3^{2-} and 27% for 10 mM of HCO_3^-. This was largely due to the fact that the scavenging effect with •OH for HCO_3^- (k = 8.5 × 10^6 M^{-1} s^{-1}) is lower than that of CO_3^{2-} (k = 3.9 × 10^8 M^{-1} s^{-1}). This is especially so when the scavenging reaction rates with $O_2^{\bullet-}$ for HCO_3^- and CO_3^{2-} are identical.

3.8.3. Chloride (Cl^-) Ion

The presence of Cl^- lowered the rate of CBZ degradation, as shown in Figure 10E,F, with k_{Obs} decreasing by roughly 26% for 2.5 mM, 54% for 15 mM, and 62% for 30 mM. Under UV-A irradiation, Cl^- has been studied as an inhibitor of titanium dioxide-based photocatalytic oxidation processes [82]. This is due to the photo-generated holes and •OH scavenging properties. Equations (17) and (18) exhibit the formulae for h_{VB}^+ scavenging [83]:

$$Cl^- + h_{VB}^+ \rightarrow Cl^{\bullet} \quad (17)$$

$$Cl^{\bullet} + Cl^- \rightarrow Cl_2^{\bullet-} \quad (18)$$

Equations (19) and (20) illustrate the equations for •OH scavenging [84]:

$$Cl^{\bullet} + \bullet OH \rightarrow ClOH^{\bullet-} \quad (19)$$

$$ClOH^{\bullet-} + Cl^- \rightarrow Cl_2^{\bullet-} + OH^- \quad (20)$$

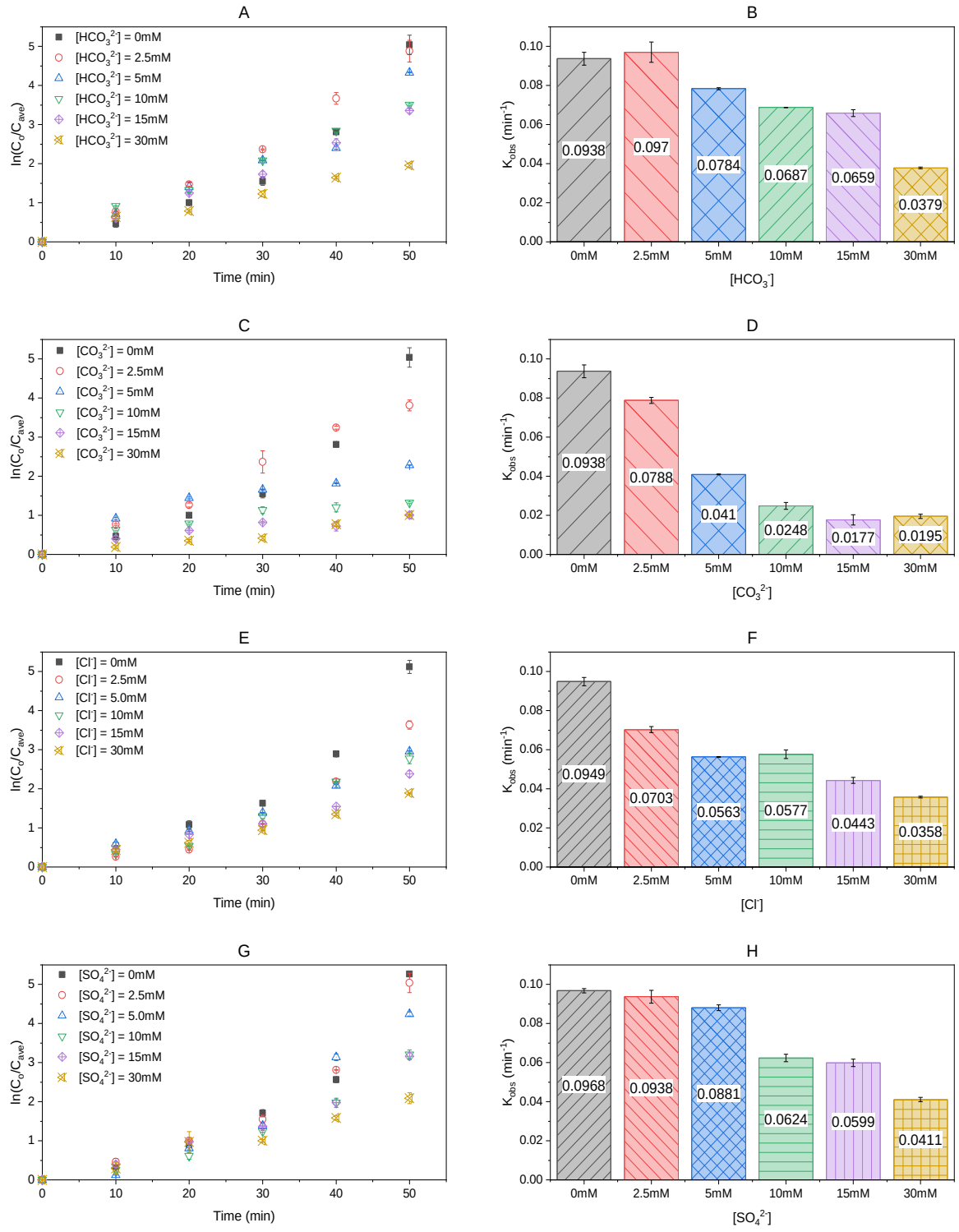

Figure 10. (**A**) ln (C_o/C_{ave}) against time and (**B**) k_{obs}, min^{-1} for varied [HCO_3^-] conditions; (**C**) ln (C_o/C_{ave}) against time and (**D**) k_{obs}, min^{-1} for varied [CO_3^{2-}] conditions; (**E**) ln (C_o/C_{ave}) against time and (**F**) k_{obs}, min^{-1} for varied [Cl^-] conditions; and (**G**) ln (C_o/C_{ave}) against time and (**H**) k_{obs}, min^{-1} for varied [SO_4^{2-}] conditions.

Chlorine radicals are also very likely to react instantly with photo-generated electrons and be converted back to chloride anions [85]. Consequently, this limits the availability of photo-generated electrons, holes, and •OH, all of which play crucial roles in the degradation of CBZ under UV-A/MIL-101(Cr)@TiO_2 conditions.

Moreover, the reactivity of Cl_2^- with CBZ is $k_{Cl2\bullet-}$ =<5 × 10^7 M^{-1} s^{-1} [86], which is significantly lower than the reactivity of ROS in the system (k > 10^9) [82]. In comparable investigations, a stronger inhibition at higher Cl^- ion concentrations was reported due to the scavenging interactions with holes and electrons [82]. Notably, the inhibitory impact of Cl^- is not as pronounced as that of alkalinity (HCO_3^- and CO_3^{2-}). They have direct scavenging effects on both $O_2^{\bullet-}$ and •OH radicals, whereas Cl^- primarily scavenges •OH radicals, since its interaction with $O_2^{\bullet-}$ is extremely slow (k < 0.014 M^{-1} s^{-1}) [79].

3.8.4. Sulphate (SO_4^{2-}) Ion

According to Equations (21)–(23), the addition of SO_4^{2-} will inhibit the degradation of CBZ due to the scavenging of photo-generated holes (h^+) and •OH, as shown in Figure 10G,H [82,84]. The decrease in the degradation rate was ~9%, ~35%, ~38%, and ~58% for 5 mM, 10 mM, 15 mM, and 30 mM, respectively.

$$SO_4^{2-} + h_{VB}^+ \rightarrow SO_4^{\bullet-} \quad (21)$$

$$SO_4^{2-} + \bullet OH \rightarrow SO_4^{\bullet-} + OH^- \quad (22)$$

$$SO_4^{\bullet-} + e_{CB}^- \rightarrow SO_4^{2-} \quad (23)$$

As a result, there were fewer photo-generated holes (h^+) and •OH available for the degradation of CBZ. Furthermore, the reactivity of $SO_4^{\bullet-}$ with CBZ ($k_{SO4\bullet-}$ = 6.83 × 10^8 M^{-1} s^{-1}) [87] was significantly lower than that of the ROS in the system (k > 10^9 M^{-1} s^{-1}), such as •OH radicals ($k_{\bullet OH}$ = 4.63 × 10^9) [87] that have been scavenged away.

Figure 10A–H illustrates the scavenging effects of the inorganic ions (SO_4^{2-}, Cl^-, CO_3^{2-}, and HCO_3^-) on CBZ degradation. When inorganic radicals developed after scavenging ROS, the scavenging effect was comparable. These inorganic radicals reacted with CBZ less quickly than the ROS species. For instance, SO_4^{2-}, Cl^-, and HCO_3^- formed the inorganic radicals $SO_4^{\bullet-}$, $Cl_2^{\bullet-}$, and $CO_3^{\bullet-}$, which have the following reactivities with CBZ: $k_{SO4\bullet-}$ = 6.83 × 10^8 M^{-1} s^{-1}, $k_{Cl2\bullet-}$ = <5 × 10^7 M^{-1} s^{-1}, and $k_{CO3\bullet-}$ = (2.3–4.2) × 10^6 M^{-1} s^{-1}. These reactivities with CBZ can also be demonstrated by their redox potentials (Table S13). The decrease in reactivity due to the formation of $CO_3^{\bullet-}$ is only more pronounced under the presence of CO_3^{2-}, as CO_3^{2-} is a more potent scavenger than HCO_3^-. This explains the greater degree of inhibition shown in Figure 10A–H.

3.9. Effects of Pharmaceutical Organic Solvents

It is necessary to examine the effects of pharmaceutical organic solvents as potential scavengers on the photocatalytic degradation of CBZ using the MIL-101(Cr)@TiO_2 composite, given the copious amount of organic solvents identified in pharmaceutical wastewater [33].

3.9.1. N, N Dimethyl Formamide (DMF)

Figure 11A demonstrates that DMF had a scavenging impact on the overall degradation of CBZ. The k_{Obs} decreased from 0.0828 min^{-1} (0 mM DMF) to 0.0421 min^{-1} (30 mM DMF). This was due to its reactivity with •OH ($k_{\bullet OH}$ = 1.7 × 10^9 M^{-1} s^{-1}) [88], which was comparable to CBZ's reactivity with •OH ($k_{\bullet OH}$ = 8.8 × 10^9 M^{-1} s^{-1}) [81]. As demonstrated in Figure S11, degradation intermediates of DMF could be observed and quantified. The degradation pathway of DMF has been commonly proposed with the subsequent formation of N-methyl formamide (NMF) and formamide [89–91]. As seen in Table S14, DMF, NMF, and formamide react well with •OH radicals [88]. However, NMF is the only intermediate of the reaction. This may suggest again that $O_2^{\bullet-}$ is more abundant than •OH in the UV-A/MIL-101(Cr)@TiO_2.

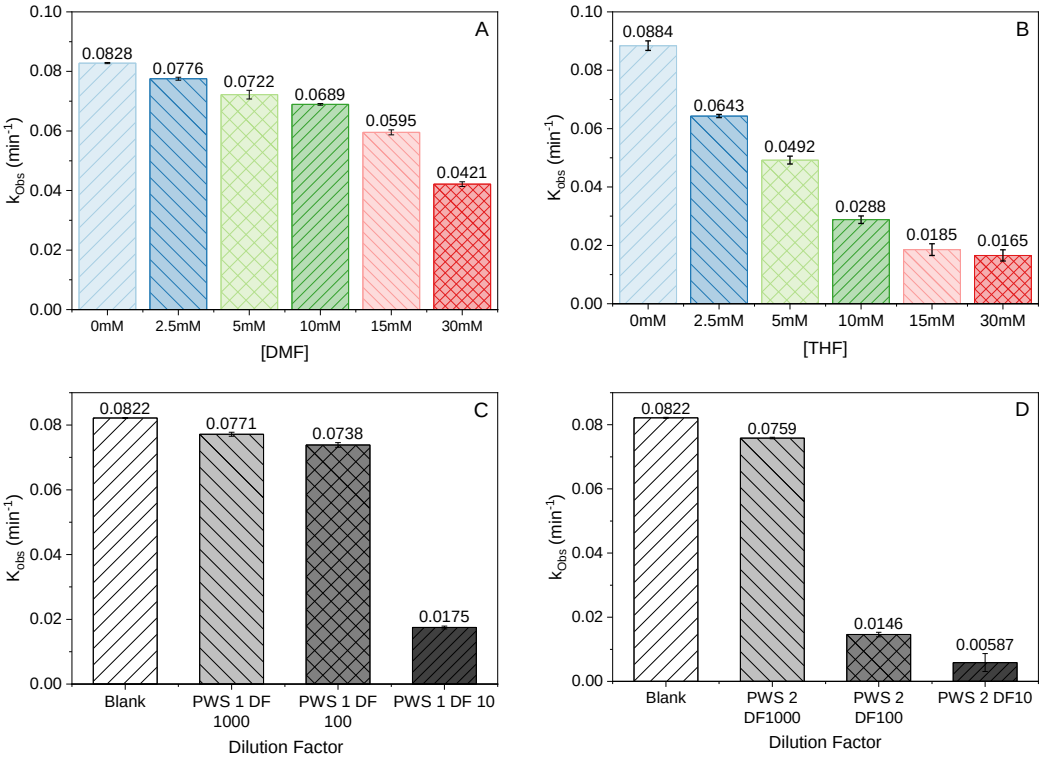

Figure 11. k_{obs}, min^{-1} for (**A**) varied concentrations of DMF, (**B**) varied concentrations of THF, (**C**) different dilution factors of PWS 1, and (**D**) different dilution factors of PWS 2.

3.9.2. Tetrahydrofuran (THF)

As seen in Figure 11B, THF also had a scavenging effect on the photodegradation of CBZ, with THF being marginally more significant. The k_{Obs} decreased from 0.0884 min^{-1} (0 mM THF) to 0.0165 min^{-1} (30 mM THF). The photocatalytic degradation of THF with a photocatalyst has been studied earlier, and superoxide radicals $O_2^{\bullet -}$ played a crucial part in the initial oxidation stage of THF [92]. Other oxygen species, such as OH• and HOO• radicals, have been identified to be responsible for the oxidation of THF to γ-butyrolactone (Figure S12) [93]. Figure S13 reveals that THF was definitely degrading; nevertheless, the intermediates were not detected by GC/MS, although the literature suggests them being γ-butyrolactone. The minute drop in THF caused by UV-A alone could be attributable to the comparatively high vapor pressure of THF, which is 162.22 mmHg.

3.10. Effect of Real Pharmaceutical Wastewater Matrix

The photocatalytic degradation of CBZ by the hetero-structured MIL-101(Cr)@TiO_2 composite was subjected to varying dilution factors of pharmaceutical wastewater samples in order to determine the scavenging effects related to the constituents of the wastewater. The degradation efficiency of pharmaceutical wastewater sample PWS 1 and PWS 2 fell dramatically with decreasing dilution factors (Figure 11C,D). For PWS 1, the k_{Obs} decreased from 0.0822 min^{-1} (blank) to 0.0771 min^{-1}, 0.0738 min^{-1}, and 0.0175 min^{-1} for the dilution factors of 1000, 100, and 10, respectively. For PWS 2, the k_{Obs} decreased from 0.0822 min^{-1} (blank) to 0.0759 min^{-1}, 0.0146 min^{-1}, and 0.00587 min^{-1} for the dilution factors of 1000, 100, and 10, respectively. As determined in the earlier sections, the drop in K_{Obs} was due to the combined scavenging actions of wastewater constituents such as inorganic ions, organic solvents, and alkalinity. It may also be partially attributable to the TiO_2 surface being excessively occupied by pollutants with higher concentrations, hence lowering the number of active sites and influencing the degradation rate [72]. When impurities exceeded the capacity of the TiO_2 composite, the photonic efficiency was also affected, resulting in TiO_2 deactivation and the inadequate formation of reactive oxygen species [75]. The drop in

the rate constant (K_{obs}) was greater for PWS 2 than PWS 1 due to the higher concentrations of organic compounds (COD, TOC), total alkalinity, and total dissolved solids (TDS). It may also possibly be related to the yellow hue of PWS 2, which reduced the photocatalyst's electron excitation when a portion of UV light was absorbed [94]. Figure S14 demonstrates that PWS 2 with a dilution factor of 10 had the greatest absorbance at a wavelength of 365 nm. This supports the lowest observed reaction rate (K_{obs}) of 0.00587 min^{-1}. The other wastewater samples with varying dilution factors exhibited comparable absorbance levels at 365 nm (Figure S14), but their K_{obs} still differed, indicating that other constituents may contribute to the overall scavenging action.

3.11. Recycling Experiments for CBZ Photocatalytic Degradation

Stability and recyclability are essential for the application of photocatalysts. After photocatalytic degradation, the photocatalyst was recovered by centrifuging the solution. As depicted in Figure 12A, the MIL-101-(Cr)@TiO_2 composite exhibited excellent reusability and stability after five cycles without a substantial decrease in its photocatalytic degradation activity. As shown by the FTIR spectrum analysis (Figure 12B), the new composite did not undergo any substantial changes, confirming its durability and high stability.

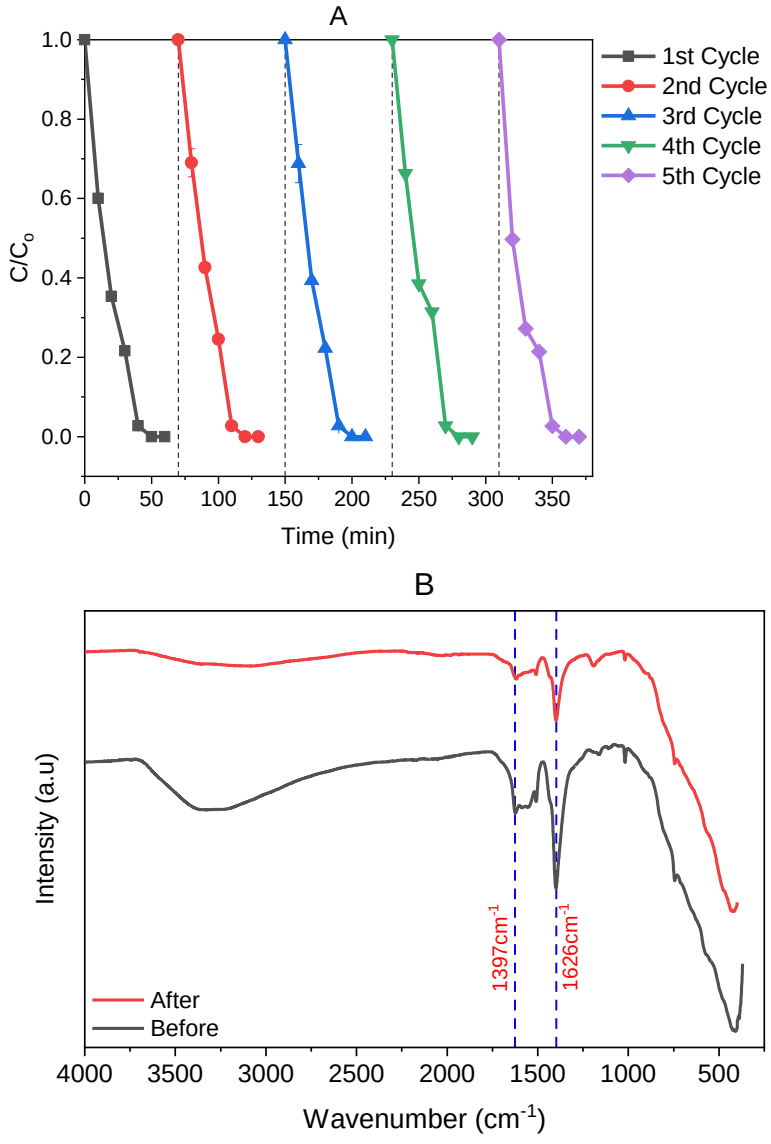

Figure 12. (**A**) Recycle experiments of MIL−101(Cr)@TiO_2 composite for CBZ degradation. (**B**) FTIR spectrum of MIL−101(Cr)@TiO_2; black: Virgin, red: after 5th cycle.

3.12. Degradation Pathways of CBZ

Using LC-MS/MS, the MS chromatogram (Figure S15) and mass spectra (Figure S16) of the CBZ intermediates were detected. The intermediates (Table S15) were determined based on their mass spectra and the literature [32,71]. The main CBZ degradation intermediates were P252 (m/z = 253) and trans-CBZ (m/z = 271). Other intermediates included hydroxylated derivatives and oxidation products, such as BQD (m/z = 267), BQM (m/z = 251), P207 (m/z = 208), acridine (m/z = 180), and acridone (m/z = 196). They are potential photocatalytic decomposition products of CBZ. To determine which ROS are responsible for the formation of intermediates, ROS quenchers were administered in excess (10 mM) to isolate intermediates. The outcomes are displayed in Table S16. Figure 13 depicts the speculated breakdown pathways of CBZ based on speculated gradation products detected by LC/MS/MS (Figure S15). The intermediates were identified owing to the isolation experiments (Table S16) and other literature.

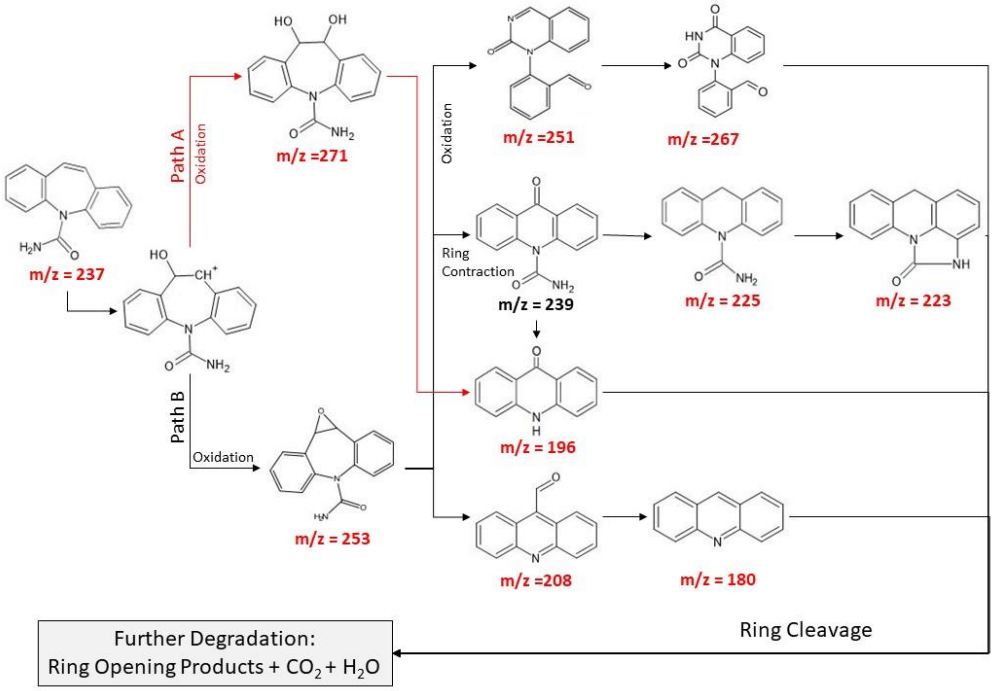

Figure 13. Proposed degradation pathways of CBZ using MIL-101(Cr)@TiO_2 under UV-A irradiation.

The radical oxygen species targeted the core heterocyclic ring's olefinic double bond. This resulted in a dihydroxyl CBZ intermediate [95,96]. The intermediate then produced epoxy-carbamazepine (P252) and 10,11–dihydroxy CBZ (trans-CBZ). Previous work frequently attributes •OH for the degradation pathway from CBZ to P252. This remained true when the compounds identified under condition III (Table S16) were CBZ (m/z = 237), P252 (m/z = 253), and P207 (m/z = 208), in which •OH is predominant and $O_2^{\bullet-}$ has been quenched. However, under condition IV (Table S16), the formation of intermediate species, P252, trans-CBZ, and other smaller organic fragments suggest that $O_2^{\bullet-}$ has an adequate oxidizing ability to break down CBZ, as previously proposed in other literature [97]. Previous studies have also reported that $O_2^{\bullet-}$ is responsible and possesses sufficient oxidising ability to cleave P252 and undergo ring contraction to create P207 [71]. Two potential reactions can lead to the synthesis of acridone (m/z = 196; P195): (Path A) successive oxidation and contraction from trans-CBZ (m/z = 271), and (Path B) a contraction of the heterocyclic ring from a seven-member ring to six-member ring to generate an intermediate (m/z = 239) and a further loss of the CHNO group [32], both of which appear to be driven by $O_2^{\bullet-}$. The production of P222 was attributed to the loss of the ketonic group and the formation of a ring (cyclization) from P224. Under condition I (Table S16), the further

decomposition of P222 into P119 has also been proposed in the literature [32]. In addition to generating BQM (m/z = 251), P252 can add oxygen to produce BQD (m/z = 267). Both stages are driven by superoxide anion radicals, $O_2^{\bullet-}$ [98]. P208 undergoes deamination and dihydroxylation to generate acridine (m/z = 180) [71]. Under condition III, the creation of P208 was discovered, and it has been proposed as an intermediate between P252 and acridine. This hypothesized degradation mechanism for the formation of P252 → P208 → acridine has been documented numerous times in the literature [71,96,99]. The CBZ intermediates BQD/P266 (m/z = 267), P222 (m/z = 223), acridone/P195 (m/z = 196), and acridine (m/z = 180) can be further oxidized to ring-rupturing compounds and complete mineralisation with the generation of CO_2 and H_2O, as shown in Figure 13 [71,96,99,100]. These ring-opening oxidation processes can be driven by oxidants such as •OH, $O_2^{\bullet-}$ and h^+ [71]. Regarding condition II (Table S16), this emphasizes the significance of h^+ in kicking off the process to produce ROS when no intermediates are formed.

4. Conclusions

This study evaluated CBZ degradation utilising UV-A/MIL-101(Cr)@TiO_2. The ideal TiO_2:MIL-101(Cr) and calcination temperature to degrade CBZ were 9.17% and 100 °C. As the TiO_2 content was increased, the BET surface area and pore volume decreased, reducing the adsorption capacity. TiO_2 improved the photocatalytic degradation until a threshold ratio, after which the adsorption and photodegradation decreased with increasing TiO_2 content. Above 100 °C, MIL-101(Cr)'s skeleton disintegrated, yielding TA with significant •OH reactivity. This resulted in a drop in the CBZ degradation rate.

The MIL-101(Cr)@TiO_2 composite displayed 99 ± 2.3% photocatalytic degradation of CBZ after 60 min compared to 84.2 ± 5.4% for TiO_2. The heterostructure delayed the photo-generated h^+ and e^- recombination and decreased the band gap. CBZ's photodegradation increased. The photocatalytic efficiency, however, was not comparable to prior investigations. The variation may be due to the lower specific surface area of HF-free MIL-101(Cr). $O_2^{\bullet-}$ was the dominant ROS in UV-A/MIL-101(Cr)@TiO_2. The calculated E_{cb} and E_{vb} for TiO_2 and MIL-101(Cr) gave a type-II heterojunction structure, which is the mechanism of UV-A/MIL-101(Cr)@TiO_2. According to the proposed mechanism, $O_2^{\bullet-}$ from MIL-101(Cr) and TiO_2 has two likely pathways.

Operating conditions such as the pH, IV intensity, composite dosage, and initial pollutant concentration were evaluated for UV-A/MIL-101(Cr)@TiO_2. The maximum degradation rate at a pH of 11 was 0.157 min^{-1}, and the lowest was at pH 3 (0.0768 min^{-1}), as OH^- enhanced the generation of •OH through photo-oxidation by h_{vb}^+. The UV intensity and composite dosage significantly affected the CBZ degradation. The initial pollutant degradation did not alter the degradation rate. This is likely due to the difference in the adsorption capacity of the composite and the fact that $O_2^{\bullet-}$ was the predominant ROS. Inorganic and organic wastewater components were analysed. HCO_3^- and CO_3^{2-} had stronger scavenging effects than Cl^- and SO_4^{2-}. THF had a marginally greater scavenging effect than DMF due to the role of $O_2^{\bullet-}$ in THF's first oxidation step. The assessment in pharmaceutical wastewater matrices revealed a dampening effect on CBZ degradation. The drop in K_{Obs} can be attributed to the wastewater constituent's scavenging effects; the composite surface being occupied by contaminants, thus limiting its active sites; or the wastewater's colour hue.

Overall, this study illustrated that UV-A/MIL-101(Cr)@TiO_2 enhanced CBZ degradation due to its Type II heterostructure by delaying electron-hole recombination and decreasing the band gap energy. Additionally, this study assessed the process feasibility in a real pharmaceutical wastewater matrix. This can be of importance with respect to future research and development in pharmaceutical wastewater treatment.

Supplementary Materials: The following supporting information can be downloaded at: https://www.mdpi.com/article/10.3390/w14233964/s1, Text S1: Chemicals & reagents; Table S1: Types of APIs identified in pharmaceutical effluents and their corresponding concentrations; Table S2: Surrogate parameters of pharmaceutical wastewater samples; Table S3: Total alkalinity as $CaCO_3$ (mg/L) of pharmaceutical wastewater samples; Table S4: Cl^- and SO_4^{2-} in pharmaceutical wastewater samples, Table S4: Cl^- and SO_4^{2-} in pharmaceutical wastewater samples; Table S5: GC/MS temperature program (DB 1301); Table S6: GC/MS temperature program (Mega-Wax); Table S7: Weight % & Atomic % of each element based on TEM EDS Point Detection Location; Table S8: Common chemical states of Cr and corresponding binding energy; Table S9: Isotherm & kinetic model parameters for adsorption of CBZ onto MIL-101(Cr); Table S10: Adsorption kinetic parameters for TiO_2: MIL-101(Cr) composites with varied ratio; Table S11: Pseudo-steady state •OH concentration [OH]ss due to TiO_2:MIL composites with varied ratio; Table S12: Rate constants for hydroxyl radical trapping ($k_{rxn/•OH}$); Table S13: Redox potentials for oxidizing species; Table S14: Rate of reaction of •OH radicals with selected amides in aqueous solution; Table S15: Possible intermediates of CBZ with their elemental composition & structure; Table S16: Intermediates identified due to various quenchers in excess at 50-minute reaction; Figure S1: GC/MS spectrum of pharmaceutical wastewater samples PWS 1 & PWS 2 using (A) DB1301, (C) Mega-Wax with MS spectrum of (B) Tetrahydrofuran & (D) N, N Dimethyl-Formamide; Figure S2: (A) Calibration curve & (B) Absorbance spectrum of CBZ by HPLC-DAD at 285nm wavelength; Figure S3: Schematic diagram of UV-A/LED photocatalytic setup; Figure S4: XPS patterns of MIL-101(Cr)@TiO_2 (Ti2p); Figure S5: XPS patterns of MIL-101(Cr)@TiO_2 (O1s); Figure S6: XPS patterns of MIL-101(Cr)@TiO_2 (Cr2p); Figure S7: XPS patterns of MIL-101(Cr)@TiO_2 (C1s); Figure S8: (A) Adsorption isotherms (B) Adsorption kinetics of CBZ on MIL-101(Cr); Figure S9: Determination of Cr concentration using ICP-OES; Figure S10: Absorbance spectra of MIL-101(Cr), MIL-101(Cr)@TiO_2 and TiO_2; Figure S11: (A) Degradation of DMF using MIL-101(Cr)@TiO_2 with the corresponding MS Spectrum (B) GC/MS spectrum at different time intervals with the presence of both DMF & N-Methyl-Formamide; Figure S12: Transformation of tetrahydrofuran to 2-hydroxytetrahydrofuran to butyrolactone; Figure S13: (A) Degradation of THF using MIL-101(Cr)@TiO_2 (B) GC/MS Spectrum with the corresponding MS Spectrum; Figure S14: Absorbance spectrum of pharmaceutical wastewater samples PWS 1 & PWS 2 with different dilution factors; Figure S15: MS chromatography of CBZ & its intermediates: (A) m/z = 237 (B) m/z = 253 (C) m/z = 251 (D) m/z = 271 (E) m/z = 120 (F) m/z = 223 (G) m/z = 267 (H) m/z = 180 (I) m/z = 196 (J) m/z = 225; Figure S16: MS spectrum of CBZ and its intermediates; Figure S17: Time-profiles of CBZ intermediates for MIL-101(Cr)@TiO_2 composite with UV-A irradiation (Max-Normalized). References [101–106] are cited in the supplementary materials.

Author Contributions: Conceptualization, J.W.G. and Y.X.; methodology, J.W.G. and Y.X.; validation, J.W.G. and Y.X.; formal analysis, J.W.G. and Y.X.; investigation, J.W.G. and Y.X.; writing – original draft preparation, J.W.G. and Y.X.; writing- review and editing, J.W.G., Y.X. and J.Y.H.; supervision, W.W., Z.H., S.L.O. and J.Y.H.; project administration, J.W.G. and J.Y.H. All authors have read and agreed to the published version of the manuscript.

Funding: This research was funded by Singapore Institute of Manufacturing Technology.

Acknowledgments: The authors would like to thank the Simtech research project for their financial support.

Conflicts of Interest: The authors declare no conflict of interest.

References

1. Long, Z.; Li, Q.; Wei, T.; Zhang, G.; Ren, Z. Historical development and prospects of photocatalysts for pollutant removal in water. *J. Hazard. Mater.* **2020**, *395*, 122599. [CrossRef] [PubMed]
2. Wen, M.; Mori, K.; Kamegawa, T.; Yamashita, H. Amine-functionalized MIL-101 (Cr) with imbedded platinum nanoparticles as a durable photocatalyst for hydrogen production from water. *Chem. Commun.* **2014**, *50*, 11645–11648. [CrossRef] [PubMed]
3. Li, X.; Pi, Y.; Xia, Q.; Li, Z.; Xiao, J. TiO_2 encapsulated in Salicylaldehyde-NH2-MIL-101 (Cr) for enhanced visible light-driven photodegradation of MB. *Appl. Catal. B Environ.* **2016**, *191*, 192–201. [CrossRef]
4. Wang, Y.; Zhang, Y.; Jiang, Z.; Jiang, G.; Zhao, Z.; Wu, Q.; Liu, Y.; Xu, Q.; Duan, A.; Xu, C. Controlled fabrication and enhanced visible-light photocatalytic hydrogen production of Au@ CdS/MIL-101 heterostructure. *Appl. Catal. B Environ.* **2016**, *185*, 307–314. [CrossRef]

5. Gao, S.; Feng, T.; Feng, C.; Shang, N.; Wang, C. Novel visible-light-responsive Ag/AgCl@ MIL-101 hybrid materials with synergistic photocatalytic activity. *J. Colloid Interface Sci.* **2016**, *466*, 284–290. [CrossRef] [PubMed]
6. Guo, F.; Yang, S.; Liu, Y.; Wang, P.; Huang, J.; Sun, W.-Y. Size Engineering of Metal–Organic Framework MIL-101 (Cr)–Ag Hybrids for Photocatalytic CO2 Reduction. *ACS Catal.* **2019**, *9*, 8464–8470. [CrossRef]
7. Mehrabadi, Z.; Faghihian, H. Comparative photocatalytic performance of TiO_2 supported on clinoptilolite and TiO_2/Salicylaldehyde-NH2-MIL-101 (Cr) for degradation of pharmaceutical pollutant atenolol under UV and visible irradiations. *J. Photochem. Photobiol. Chem.* **2018**, *356*, 102–111. [CrossRef]
8. Xu, Y.; Lv, M.; Yang, H.; Chen, Q.; Liu, X.; Wei, F. BiVO 4/MIL-101 composite having the synergistically enhanced visible light photocatalytic activity. *RSC Adv.* **2015**, *5*, 43473–43479. [CrossRef]
9. Pi, Y.; Li, X.; Xia, Q.; Wu, J.; Li, Y.; Xiao, J.; Li, Z. Adsorptive and photocatalytic removal of Persistent Organic Pollutants (POPs) in water by metal-organic frameworks (MOFs). *Chem. Eng. J.* **2018**, *337*, 351–371. [CrossRef]
10. Hasan, Z.; Choi, E.-J.; Jhung, S.H. Adsorption of naproxen and clofibric acid over a metal–organic framework MIL-101 functionalized with acidic and basic groups. *Chem. Eng. J.* **2013**, *219*, 537–544. [CrossRef]
11. Jhung, S.H.; Lee, J.-H.; Yoon, J.W.; Serre, C.; Férey, G.; Chang, J.-S. Microwave synthesis of chromium terephthalate MIL-101 and its benzene sorption ability. *Adv. Mater.* **2007**, *19*, 121–124. [CrossRef]
12. Chen, C.; Zhang, M.; Guan, Q.; Li, W. Kinetic and thermodynamic studies on the adsorption of xylenol orange onto MIL-101 (Cr). *Chem. Eng. J.* **2012**, *183*, 60–67. [CrossRef]
13. Haque, E.; Lee, J.E.; Jang, I.T.; Hwang, Y.K.; Chang, J.-S.; Jegal, J.; Jhung, S.H. Adsorptive removal of methyl orange from aqueous solution with metal-organic frameworks, porous chromium-benzenedicarboxylates. *J. Hazard. Mater.* **2010**, *181*, 535–542. [CrossRef] [PubMed]
14. Sun, X.; Xia, Q.; Zhao, Z.; Li, Y.; Li, Z. Synthesis and adsorption performance of MIL-101 (Cr)/graphite oxide composites with high capacities of n-hexane. *Chem. Eng. J.* **2014**, *239*, 226–232. [CrossRef]
15. Karmakar, S.; Roy, D.; Janiak, C.; De, S. Insights into multi-component adsorption of reactive dyes on MIL-101-Cr metal organic framework: Experimental and modeling approach. *Sep. Purif. Technol.* **2019**, *215*, 259–275. [CrossRef]
16. Wang, Y.; Dai, X.; He, X.; Chen, L.; Hou, X. MIL-101 (Cr)@ GO for dispersive micro-solid-phase extraction of pharmaceutical residue in chicken breast used in microwave-assisted coupling with HPLC–MS/MS detection. *J. Pharm. Biomed. Anal.* **2017**, *145*, 440–446. [CrossRef]
17. Leng, F.; Wang, W.; Zhao, X.J.; Hu, X.L.; Li, Y.F. Adsorption interaction between a metal–organic framework of chromium–benzenedicarboxylates and uranine in aqueous solution. *Colloids Surf. Physicochem. Eng. Asp.* **2014**, *441*, 164–169. [CrossRef]
18. Gao, Y.; Liu, K.; Kang, R.; Xia, J.; Yu, G.; Deng, S. A comparative study of rigid and flexible MOFs for the adsorption of pharmaceuticals: Kinetics, isotherms and mechanisms. *J. Hazard. Mater.* **2018**, *359*, 248–257. [CrossRef]
19. Férey, G.; Mellot-Draznieks, C.; Serre, C.; Millange, F.; Dutour, J.; Surblé, S.; Margiolaki, I. A chromium terephthalate-based solid with unusually large pore volumes and surface area. *Science* **2005**, *309*, 2040–2042. [CrossRef]
20. Metcalfe, C.D.; Koenig, B.G.; Bennie, D.T.; Servos, M.; Ternes, T.A.; Hirsch, R. Occurrence of neutral and acidic drugs in the effluents of Canadian sewage treatment plants. *Environ. Toxicol. Chem. Int. J.* **2003**, *22*, 2872–2880. [CrossRef]
21. Metcalfe, C.D.; Miao, X.-S.; Koenig, B.G.; Struger, J. Distribution of acidic and neutral drugs in surface waters near sewage treatment plants in the lower Great Lakes, Canada. *Environ. Toxicol. Chem. Int. J.* **2003**, *22*, 2881–2889. [CrossRef]
22. De Voogt, P.; Janex-Habibi, M.-L.; Sacher, F.; Puijker, L.; Mons, M. Development of a common priority list of pharmaceuticals relevant for the water cycle. *Water Sci. Technol.* **2009**, *59*, 39–46. [CrossRef] [PubMed]
23. Daughton, C.G.; Jones-Lepp, T.L. *Pharmaceuticals and Personal Care Products in the Environment*; American Chemical Society: New York, NY, USA, 2001.
24. Larsson, D.G.J. Drug production facilities–an overlooked discharge source for pharmaceuticals to the environment. In *Pharmaceuticals in the Environment*; Springer: Berlin/Heidelberg, Germany, 2008; pp. 37–42.
25. Dwivedi, K.; Morone, A.; Pratape, V.; Chakrabarti, T.; Pandey, R.A. Carbamazepine and oxcarbazepine removal in pharmaceutical wastewater treatment plant using a mass balance approach: A case study. *Korean J. Chem. Eng.* **2017**, *34*, 2662–2671. [CrossRef]
26. Lester, Y.; Mamane, H.; Zucker, I.; Avisar, D. Treating wastewater from a pharmaceutical formulation facility by biological process and ozone. *Water Res.* **2013**, *47*, 4349–4356. [CrossRef] [PubMed]
27. Olvera-Vargas, H.; Gore-Datar, N.; Garcia-Rodriguez, O.; Mutnuri, S.; Lefebvre, O. Electro-Fenton treatment of real pharmaceutical wastewater paired with a BDD anode: Reaction mechanisms and respective contribution of homogeneous and heterogeneous OH. *Chem. Eng. J.* **2021**, *404*, 126524. [CrossRef]
28. Sim, W.-J.; Lee, J.-W.; Lee, E.-S.; Shin, S.-K.; Hwang, S.-R.; Oh, J.-E. Occurrence and distribution of pharmaceuticals in wastewater from households, livestock farms, hospitals and pharmaceutical manufactures. *Chemosphere* **2011**, *82*, 179–186. [CrossRef]
29. Ternes, T.A. Occurrence of drugs in German sewage treatment plants and rivers. *Water Res.* **1998**, *32*, 3245–3260. [CrossRef]
30. Chang, N.; Zhang, H.; Shi, M.-S.; Li, J.; Shao, W.; Wang, H.-T. Metal-organic framework templated synthesis of TiO_2@ MIL-101 core-shell architectures for high-efficiency adsorption and photocatalysis. *Mater. Lett.* **2017**, *200*, 55–58. [CrossRef]
31. Tang, Y.; Yin, X.; Mu, M.; Jiang, Y.; Li, X.; Zhang, H.; Ouyang, T. Anatase TiO_2@ MIL-101 (Cr) nanocomposite for photocatalytic degradation of bisphenol A. *Colloids Surf. Physicochem. Eng. Asp.* **2020**, *596*, 124745. [CrossRef]
32. Franz, S.; Falletta, E.; Arab, H.; Murgolo, S.; Bestetti, M.; Mascolo, G. Degradation of carbamazepine by photo (electro) catalysis on nanostructured TiO_2 meshes: Transformation products and reaction pathways. *Catalysts* **2020**, *10*, 169. [CrossRef]

33. Gadipelly, C.; Pérez-González, A.; Yadav, G.D.; Ortiz, I.; Ibáñez, R.; Rathod, V.K.; Marathe, K.V. Pharmaceutical industry wastewater: Review of the technologies for water treatment and reuse. *Ind. Eng. Chem. Res.* **2014**, *53*, 11571–11592. [CrossRef]
34. Guo, Y.; Qi, P.S.; Liu, Y.Z. A review on advanced treatment of pharmaceutical wastewater. *IOP Conf. Ser. Earth Environ. Sci.* **2017**, *63*, 012025. [CrossRef]
35. Shi, X.; Leong, K.Y.; Ng, H.Y. Anaerobic treatment of pharmaceutical wastewater: A critical review. *Bioresour. Technol.* **2017**, *245*, 1238–1244. [CrossRef] [PubMed]
36. Rana, R.S.; Singh, P.; Kandari, V.; Singh, R.; Dobhal, R.; Gupta, S. A review on characterization and bioremediation of pharmaceutical industries' wastewater: An Indian perspective. *Appl. Water Sci.* **2017**, *7*, 1–12. [CrossRef]
37. Kayal, S.; Sun, B.; Chakraborty, A. Study of metal-organic framework MIL-101 (Cr) for natural gas (methane) storage and compare with other MOFs (metal-organic frameworks). *Energy* **2015**, *91*, 772–781. [CrossRef]
38. Tauc, J.; Grigorovici, R.; Vancu, A. Optical properties and electronic structure of amorphous germanium. *Phys. Status Solidi B* **1966**, *15*, 627–637. [CrossRef]
39. Kumar, K.V.; Porkodi, K.; Rocha, F. Langmuir–Hinshelwood kinetics–a theoretical study. *Catal. Commun.* **2008**, *9*, 82–84. [CrossRef]
40. Elovitz, M.S.; von Gunten, U. Hydroxyl radical/ozone ratios during ozonation processes. I. The R_{ct} concept. *Ozone Sci. Eng.* **1999**, *21*, 239–260. [CrossRef]
41. Fang, Y.; Zhao, G.; Dai, W.; Ma, L.; Ma, N. Enhanced adsorption of rubidium ion by a phenol@ MIL-101 (Cr) composite material. *Microporous Mesoporous Mater.* **2017**, *251*, 51–57. [CrossRef]
42. Kayal, S.; Chakraborty, A. Activated carbon (type Maxsorb-III) and MIL-101 (Cr) metal organic framework based composite adsorbent for higher CH4 storage and CO2 capture. *Chem. Eng. J.* **2018**, *334*, 780–788. [CrossRef]
43. Maksimchuk, N.; Timofeeva, M.; Mel'Gunov, M.; Shmakov, A.; Chesalov, Y.; Dybtsev, D.; Fedin, V.; Kholdeeva, O. Heterogeneous selective oxidation catalysts based on coordination polymer MIL-101 and transition metal-substituted polyoxometalates. *J. Catal.* **2008**, *257*, 315–323. [CrossRef]
44. Rodrigues, M.A.; Ribeiro, J.D.; Costa, E.D.; de Miranda, J.L.; Ferraz, H.C. Nanostructured membranes containing UiO-66 (Zr) and MIL-101 (Cr) for O2/N2 and CO2/N2 separation. *Sep. Purif. Technol.* **2018**, *192*, 491–500. [CrossRef]
45. Chang, N.; He, D.-Y.; Li, Y.-X.; Tang, Z.-W.; Huang, Y.-F. Fabrication of TiO 2@ MIL-53 core–shell composite for exceptionally enhanced adsorption and degradation of nonionic organics. *RSC Adv.* **2016**, *6*, 71481–71484. [CrossRef]
46. Jarrah, A.; Farhadi, S. K 6 P 2 W 18 O 62 encapsulated into magnetic Fe 3 O 4/MIL-101 (Cr) metal–organic framework: A novel magnetically recoverable nanoporous adsorbent for ultrafast treatment of aqueous organic pollutants solutions. *RSC Adv.* **2018**, *8*, 37976–37992. [CrossRef]
47. Jarrah, A.; Farhadi, S. Dawson-type polyoxometalate incorporated into nanoporous mil-101 (cr): Preparation, characterization and application for ultrafast removal of organic dyes. *Acta Chim. Slov.* **2019**, *66*, 85–102. [CrossRef]
48. Sheng, H.; Chen, D.; Li, N.; Xu, Q.; Li, H.; He, J.; Lu, J. Urchin-inspired TiO_2@ MIL-101 double-shell hollow particles: Adsorption and highly efficient photocatalytic degradation of hydrogen sulfide. *Chem. Mater.* **2017**, *29*, 5612–5616. [CrossRef]
49. Wu, W.; Yao, T.; Xiang, Y.; Zou, H.; Zhou, Y. Efficient removal of methyl orange by a flower-like TiO 2/MIL-101 (Cr) composite nanomaterial. *Dalton Trans.* **2020**, *49*, 5722–5729. [CrossRef]
50. Guo, H.; Wang, D.; Chen, J.; Weng, W.; Huang, M.; Zheng, Z. Simple fabrication of flake-like NH2-MIL-53 (Cr) and its application as an electrochemical sensor for the detection of Pb2+. *Chem. Eng. J.* **2016**, *289*, 479–485. [CrossRef]
51. Luo, X.-P.; Fu, S.-Y.; Du, Y.-M.; Guo, J.-Z.; Li, B. Adsorption of methylene blue and malachite green from aqueous solution by sulfonic acid group modified MIL-101. *Microporous Mesoporous Mater.* **2017**, *237*, 268–274. [CrossRef]
52. Rallapalli, P.B.; Raj, M.C.; Senthilkumar, S.; Somani, R.S.; Bajaj, H.C. HF-free synthesis of MIL-101 (Cr) and its hydrogen adsorption studies. *Environ. Prog. Sustain. Energy* **2016**, *35*, 461–468. [CrossRef]
53. Zhang, L.J.; Li, F.Q.; Ren, J.X.; Ma, L.B.; Li, M.Q. Preparation of metal organic frameworks MIL-101 (Cr) with acetic acid as mineralizer. *IOP Conf. Ser. Earth Environ. Sci.* **2018**, *199*, 042038. [CrossRef]
54. Dai, C.; Zhou, X.; Zhang, Y.; Duan, Y.; Qiang, Z.; Zhang, T.C. Comparative study of the degradation of carbamazepine in water by advanced oxidation processes. *Environ. Technol.* **2012**, *33*, 1101–1109. [CrossRef] [PubMed]
55. Doudrick, K.; Monzón, O.; Mangonon, A.; Hristovski, K.; Westerhoff, P. Nitrate reduction in water using commercial titanium dioxide photocatalysts (P25, P90, and Hombikat UV100). *J. Environ. Eng.* **2012**, *138*, 852–861. [CrossRef]
56. Oveisi, M.; Asli, M.A.; Mahmoodi, N.M. MIL-Ti metal-organic frameworks (MOFs) nanomaterials as superior adsorbents: Synthesis and ultrasound-aided dye adsorption from multicomponent wastewater systems. *J. Hazard. Mater.* **2018**, *347*, 123–140. [CrossRef] [PubMed]
57. Zhao, H.; Li, Q.; Wang, Z.; Wu, T.; Zhang, M. Synthesis of MIL-101 (Cr) and its water adsorption performance. *Microporous Mesoporous Mater.* **2020**, *297*, 110044. [CrossRef]
58. Jing, Y.; Chaplin, B.P. Mechanistic study of the validity of using hydroxyl radical probes to characterize electrochemical advanced oxidation processes. *Environ. Sci. Technol.* **2017**, *51*, 2355–2365. [CrossRef]
59. Basheer, C. Application of titanium dioxide-graphene composite material for photocatalytic degradation of alkylphenols. *J. Chem.* **2013**, *2013*, 1–10. [CrossRef]
60. Yu, Y.; Yu, J.C.; Yu, J.-G.; Kwok, Y.-C.; Che, Y.-K.; Zhao, J.-C.; Ding, L.; Ge, W.-K.; Wong, P.-K. Enhancement of photocatalytic activity of mesoporous TiO_2 by using carbon nanotubes. *Appl. Catal. Gen.* **2005**, *289*, 186–196. [CrossRef]

61. He, J.; Yan, Z.; Wang, J.; Xie, J.; Jiang, L.; Shi, Y.; Yuan, F.; Yu, F.; Sun, Y. Significantly enhanced photocatalytic hydrogen evolution under visible light over CdS embedded on metal–organic frameworks. *Chem. Commun.* **2013**, *49*, 6761–6763. [CrossRef]
62. Siadatnasab, F.; Farhadi, S.; Hoseini, A.-A.; Sillanpää, M. Synthesis and characterization of a novel manganese ferrite–metal organic framework MIL-101 (Cr) nanocomposite as an efficient and magnetically recyclable sonocatalyst. *New J. Chem.* **2020**, *44*, 16234–16245. [CrossRef]
63. Thanh, H.T.M.; Tu, N.T.T.; Hung, N.P.; Tuyen, T.N.; Mau, T.X.; Khieu, D.Q. Magnetic iron oxide modified MIL-101 composite as an efficient visible-light-driven photocatalyst for methylene blue degradation. *J. Porous Mater.* **2019**, *26*, 1699–1712. [CrossRef]
64. Putz, M.V. Path integrals for electronic densities, reactivity indices, and localization functions in quantum systems. *Int. J. Mol. Sci.* **2009**, *10*, 4816–4940. [CrossRef] [PubMed]
65. Bledowski, M.; Wang, L.; Ramakrishnan, A.; Khavryuchenko, O.V.; Khavryuchenko, V.D.; Ricci, P.C.; Strunk, J.; Cremer, T.; Kolbeck, C.; Beranek, R. Visible-light photocurrent response of TiO 2–polyheptazine hybrids: Evidence for interfacial charge-transfer absorption. *Phys. Chem. Chem. Phys.* **2011**, *13*, 21511–21519. [CrossRef] [PubMed]
66. Lu, J.; Jin, H.; Dai, Y.; Yang, K.; Huang, B. Effect of Electronegativity and Charge Balance on the Visible-Light-Responsive Photocatalytic Activity of Nonmetal Doped Anatase TiO_2. *Int. J. Photoenergy* **2011**, *2012*, 928503. [CrossRef]
67. Constantin, M.A.; Chiriac, F.L.; Gheorghe, S.; Constantin, L.A. Degradation of carbamazepine from aqueous solutions via TiO_2-assisted photo catalyze. *Toxics* **2022**, *10*, 168. [CrossRef]
68. Bielski, B.H.; Allen, A.O. Mechanism of the disproportionation of superoxide radicals. *J. Phys. Chem.* **1977**, *81*, 1048–1050. [CrossRef]
69. Wang, Z.; Ma, W.; Chen, C.; Ji, H.; Zhao, J. Probing paramagnetic species in titania-based heterogeneous photocatalysis by electron spin resonance (ESR) spectroscopy—A mini review. *Chem. Eng. J.* **2011**, *170*, 353–362. [CrossRef]
70. Dvoranová, D.; Barbieriková, Z.; Brezová, V. Radical intermediates in photoinduced reactions on TiO_2 (an EPR spin trapping study). *Molecules* **2014**, *19*, 17279–17304. [CrossRef]
71. Yang, L.; Hao, X.; Yu, D.; Zhou, P.; Peng, Y.; Jia, Y.; Lai, B. High visible-light catalytic activity of Bis-PDI-T@ TiO_2 for activating persulfate toward efficient degradation of carbamazepine. *Sep. Purif. Technol.* **2021**, *263*, 118384. [CrossRef]
72. Carabin, A.; Drogui, P.; Robert, D. Photo-degradation of carbamazepine using TiO_2 suspended photocatalysts. *J. Taiwan Inst. Chem. Eng.* **2015**, *54*, 109–117. [CrossRef]
73. Vogna, D.; Marotta, R.; Andreozzi, R.; Napolitano, A.; d'Ischia, M. Kinetic and chemical assessment of the UV/H2O2 treatment of antiepileptic drug carbamazepine. *Chemosphere* **2004**, *54*, 497–505. [CrossRef] [PubMed]
74. Ran, Z.; Fang, Y.; Sun, J.; Ma, C.; Li, S. Photocatalytic oxidative degradation of carbamazepine by TiO_2 irradiated by UV light emitting diode. *Catalysts* **2020**, *10*, 540. [CrossRef]
75. Im, J.-K.; Son, H.-S.; Kang, Y.-M.; Zoh, K.-D. Carbamazepine degradation by photolysis and titanium dioxide photocatalysis. *Water Environ. Res.* **2012**, *84*, 554–561. [CrossRef] [PubMed]
76. Chong, M.N.; Jin, B.; Chow, C.W.; Saint, C. Recent developments in photocatalytic water treatment technology: A review. *Water Res.* **2010**, *44*, 2997–3027. [CrossRef]
77. Malato, S.; Fernández-Ibáñez, P.; Maldonado, M.I.; Blanco, J.; Gernjak, W. Decontamination and disinfection of water by solar photocatalysis: Recent overview and trends. *Catal. Today* **2009**, *147*, 1–59. [CrossRef]
78. Wang, N.; Li, X.; Wang, Y.; Quan, X.; Chen, G. Evaluation of bias potential enhanced photocatalytic degradation of 4-chlorophenol with TiO_2 nanotube fabricated by anodic oxidation method. *Chem. Eng. J.* **2009**, *146*, 30–35. [CrossRef]
79. Bielski, B.H.; Cabelli, D.E.; Arudi, R.L.; Ross, A.B. Reactivity of HO2/O- 2 radicals in aqueous solution. *J. Phys. Chem. Ref. Data* **1985**, *14*, 1041–1100. [CrossRef]
80. Buxton, G.V.; Greenstock, C.L.; Helman, W.P.; Ross, A.B. Critical review of rate constants for reactions of hydrated electrons, hydrogen atoms and hydroxyl radicals (· OH/· O- in aqueous solution. *J. Phys. Chem. Ref. Data* **1988**, *17*, 513–886. [CrossRef]
81. Mandal, S. Reaction rate constants of hydroxyl radicals with micropollutants and their significance in advanced oxidation processes. *J. Adv. Oxid. Technol.* **2018**, *21*, 178–195. [CrossRef]
82. Dugandžić, A.M.; Tomašević, A.V.; Radišić, M.M.; Šekuljica, N.Ž.; Mijin, D.Ž.; Petrović, S.D. Effect of inorganic ions, photosensitisers and scavengers on the photocatalytic degradation of nicosulfuron. *J. Photochem. Photobiol. Chem.* **2017**, *336*, 146–155. [CrossRef]
83. Neppolian, B.; Choi, H.C.; Sakthivel, S.; Arabindoo, B.; Murugesan, V. Solar light induced and TiO_2 assisted degradation of textile dye reactive blue 4. *Chemosphere* **2002**, *46*, 1173–1181. [CrossRef] [PubMed]
84. Santiago, D.E.; Araña, J.; González-Díaz, O.; Alemán-Dominguez, M.; Acosta-Dacal, A.C.; Fernandez-Rodríguez, C.; Pérez-Peña, J.; Doña-Rodríguez, J.M. Effect of inorganic ions on the photocatalytic treatment of agro-industrial wastewaters containing imazalil. *Appl. Catal. B Environ.* **2014**, *156*, 284–292. [CrossRef]
85. Lair, A.; Ferronato, C.; Chovelon, J.-M.; Herrmann, J.-M. Naphthalene degradation in water by heterogeneous photocatalysis: An investigation of the influence of inorganic anions. *J. Photochem. Photobiol. Chem.* **2008**, *193*, 193–203. [CrossRef]
86. Wojnárovits, L.; Takács, E. Rate constants of dichloride radical anion reactions with molecules of environmental interest in aqueous solution: A review. *Environ. Sci. Pollut. Res.* **2021**, *28*, 41552–41575. [CrossRef]
87. Xiao, R.; Ma, J.; Luo, Z.; Zeng, W.; Wei, Z.; Spinney, R.; Hu, W.; Dionysiou, D.D. Experimental and theoretical insight into hydroxyl and sulfate radicals-mediated degradation of carbamazepine. *Environ. Pollut.* **2020**, *257*, 113498. [CrossRef]

88. Hayon, E.; Ibata, T.; Lichtin, N.N.; Simic, M. Sites of attack of hydroxyl radicals on amides in aqueous solution. *J. Am. Chem. Soc.* **1970**, *92*, 3898–3903. [CrossRef]
89. Chen, Y.; Li, B.; Qiu, Y.; Xu, X.; Shen, S. A novel chemical/biological combined technique for N, N-dimethylformamide wastewater treatment. *Environ. Technol.* **2015**, *37*, 1088–1093. [CrossRef]
90. Hu, X.; Dong, H.; Zhang, Y.; Fang, B.; Jiang, W. Mechanism of N, N-dimethylformamide electrochemical oxidation using a Ti/RuO 2–IrO 2 electrode. *RSC Adv.* **2021**, *11*, 7205–7213. [CrossRef]
91. Kong, Z.; Li, L.; Li, Y.Y. Long-term performance of UASB in treating N, N-dimethylformamide-containing wastewater with a rapid start-up by inoculating mixed sludge. *Sci. Total Environ.* **2019**, *648*, 1141–1150. [CrossRef]
92. Mehrvar, M.; Anderson, W.A.; Moo-Young, M. Photocatalytic degradation of aqueous tetrahydrofuran, 1, 4-dioxane, and their mixture with TiO_2. *Int. J. Photoenergy* **2000**, *2*, 67–80. [CrossRef]
93. Padmalatha, P.; Khatri, P.K.; Jain, S.L. Selenium-Doped TiO_2 as an Efficient Photocatalyst for the Oxidation of Tetrahydrofuran to γ-Butyrolactone Using Hydrogen Peroxide as Oxidant. *Synlett* **2013**, *24*, 1405–1409.
94. Tichapondwa, S.M.; Newman, J.P.; Kubheka, O. Effect of TiO_2 phase on the photocatalytic degradation of methylene blue dye. *Phys. Chem. Earth Parts ABC* **2020**, *118*, 102900. [CrossRef]
95. Mohapatra, D.; Brar, S.; Daghrir, R.; Tyagi, R.; Picard, P.; Surampalli, R.; Drogui, P. Photocatalytic degradation of carbamazepine in wastewater by using a new class of whey-stabilized nanocrystalline TiO_2 and ZnO. *Sci. Total Environ.* **2014**, *485*, 263–269. [CrossRef] [PubMed]
96. Nawaz, M.; Miran, W.; Jang, J.; Lee, D.S. One-step hydrothermal synthesis of porous 3D reduced graphene oxide/TiO_2 aerogel for carbamazepine photodegradation in aqueous solution. *Appl. Catal. B Environ.* **2017**, *203*, 85–95. [CrossRef]
97. Dong, C.; Wang, Z.; Ye, Z.; He, J.; Zheng, Z.; Gong, X.; Zhang, J.; Lo, I. M Superoxide radicals dominated visible light driven peroxymonosulfate activation using molybdenum selenide (MoSe2) for boosting catalytic degradation of pharmaceuticals and personal care products. *Appl. Catal. B Environ.* **2021**, *296*, 120223. [CrossRef]
98. Mcdowell, D.C.; Huber, M.M.; Wagner, M.; von Gunten, U.; Ternes, T.A. Ozonation of carbamazepine in drinking water: Identification and kinetic study of major oxidation products. *Environ. Sci. Technol.* **2005**, *39*, 8014–8022. [CrossRef] [PubMed]
99. Xu, J.; Li, L.; Guo, C.; Zhang, Y.; Meng, W. Photocatalytic degradation of carbamazepine by tailored BiPO4: Efficiency, intermediates and pathway. *Appl. Catal. B Environ.* **2013**, *130*, 285–292. [CrossRef]
100. Gao, X.; Zhang, X.; Wang, Y.; Peng, S.; Yue, B.; Fan, C. Photocatalytic degradation of carbamazepine using hierarchical BiOCl microspheres: Some key operating parameters, degradation intermediates and reaction pathway. *Chem. Eng. J.* **2015**, *273*, 156–165. [CrossRef]
101. Page, S.E.; Arnold, W.A.; McNeill, K. Terephthalate as a probe for photochemically generated hydroxyl radical. *J. Environ. Monit.* **2010**, *12*, 1658–1665. [CrossRef] [PubMed]
102. Finkelstein, E.; Rosen, G.M.; Rauckman, E.J. Arch. Biochem. Biophys. *Arch. Biochem. Biophys.* **1980**, *200*, 1–16.
103. Nosaka, Y.; Komori, S.; Yawata, K.; Hirakawa, T.; Nosaka, A.Y.; Photocatalytic OH radical formation in TiO_2 aqueous suspension studied by several detection methods. Photocatalytic OH radical formation in TiO 2 aqueous suspension studied by several detection methods. *Phys. Chem. Chem. Phys.* **2003**, *5*, 4731–4735. [CrossRef]
104. Stemmler, A.J.; Burrows, C.J. Guanine versus deoxyribose damage in DNA oxidation mediated by vanadium (IV) and vanadium (V) complexes. *J. Biol. Inorg. Chem.* **2001**, *6*, 100–106. [CrossRef] [PubMed]
105. Huie, R.E.; Clifton, C.L.; Neta, P. Electron transfer reaction rates and equilibria of the carbonate and sulfate radical anions. *Int. J. Radiat. Appl. Instrum. Part C Radiat. Phys. Chem.* **1991**, *38*, 477–481. [CrossRef]
106. Augusto, O.; Bonini, M.G.; Amanso, A.M.; Linares, E.; Santos, C.C.; de Menezes, S.L. Nitrogen dioxide and carbonate radical anion: Two emerging radicals in biology. *Free Radic. Biol. Med.* **2002**, *32*, 841–859. [CrossRef] [PubMed]